

General Disclaimer

One or more of the Following Statements may affect this Document

- This document has been reproduced from the best copy furnished by the organizational source. It is being released in the interest of making available as much information as possible.
- This document may contain data, which exceeds the sheet parameters. It was furnished in this condition by the organizational source and is the best copy available.
- This document may contain tone-on-tone or color graphs, charts and/or pictures, which have been reproduced in black and white.
- This document is paginated as submitted by the original source.
- Portions of this document are not fully legible due to the historical nature of some of the material. However, it is the best reproduction available from the original submission.

09
A

INSTITUTE for FLUID DYNAMICS and APPLIED MATHEMATICS

Technical Note No. BN-816

January 1976

WATER VAPOR LIDAR

by

R. Ellingson, T. McIlrath,
G. Schwemmer, and T. D. Wilkerson

(NASA-CR-146340) WATER VAPOR LIDAR Final
Report (Maryland Univ.) 89 p HC \$5.00
CSCI 20E

G3/36

MAR 1976
N76-18430
THRU
N76-18433
Unclas
14242
9401723

UNIVERSITY OF MARYLAND
College Park

Technical Note No. BN-816

January 1976

WATER VAPOR LIDAR^{*}

by

R. Ellingson, T. McIlrath
G. Schwemmer, and T. D. Wilkerson

*Final Report on NASA grant NSG-1036 through the Lidar Applications Section, ESSD, NASA-Langley Research Center. This research was also supported in part by NASA grant NSG-1156, and by the University of Maryland through IFDAM, and the Graduate Program in Meteorology, and the Center for Environmental and Estuarine Studies.

TABLE OF CONTENTS

	<u>Page</u>
<u>Section 1.</u> <u>Introduction and Summary</u>	1
<u>Section 2.</u> <u>A Summary of Meteorological Requirements for Water Vapor Data and Possible Space Shuttle Applications</u>	4
2.1. Introductory Remarks.	4
2.2. Water Vapor and Temperature Measurement Requirements.	6
2.3. Current and Planned Operational Atmospheric Sounding Systems.	12
2.4. Applications of Water Vapor Profiles Obtained from the Space Shuttle Lidar	17
<u>Section 3.</u> <u>Lidar Simulation</u>	23
3.1. Preliminaries	23
3.2. Water Spectrum: Wavelengths, Strengths and Widths.	31
3.3. Results of Lidar Calculations	39
3.3.1. Uniform Atmospheres (horizontal ranging)	40
3.3.2. Detection of Humidity Variations (horizontal ranging)	48
3.3.3. Vertical Ranging from Ground Stations.	52
3.3.4. Space Shuttle (downward ranging, 200 km altitude)	62
3.4. Accuracy and Practicality of Orbital Lidar for [H ₂ O]	72
<u>Section 4.</u> <u>Exploratory Laser Experiments.</u>	76
4.1. Operation of Long Pulse Dye Laser	76
4.2. Short Pulse Flashlamp-Pumped Laser.	77
4.3. Laser-Pumped Dye Laser with Cresyl Violet	78
4.4. Laser-Pumped Dye Laser with Nile Blue Perchlorate	78
4.5. Summary	78
<u>Appendix 1.</u> <u>The Relationship Between Different Meteorological Parameters Used To Specify The Water Vapor Content of Air</u> .	80
<u>References</u>	82

WATER VAPOR LIDAR

1. Introduction and Summary

This report summarizes a study of the feasibility of measuring atmospheric water vapor by means of a tunable lidar operated from the Space Shuttle. The purpose of such measurements would be to determine vertical profiles of humidity as functions of time, place and atmospheric activity.

The specific method evaluated here is differential absorption, a "two-color" method in which the atmospheric path of interest is traversed by two laser pulses: one tuned exactly to the wavelength of a water vapor absorption line, the other tuned to a nearby wavelength in a gap in the water spectrum. Analysis of the two backscattered signals yields the number density $[H_2O]$ as a function of range along the chosen atmospheric path. Of all the range-resolving lidar methods, differential absorption is the most sensitive for measuring $[H_2O]$, $[O_3]$, $[NO_2]$, $[SO_2]$ and other molecular gases in the denser parts of the atmosphere. Thus the possibility of lidar monitoring of such atmospheric molecules from the Space Shuttle seems best evaluated from the standpoint of differential absorption.

The question of feasibility can be phrased roughly as: Can we orbit a laser radar station of sufficient power and precision that useful atmospheric humidity profiles can be retrieved from the signals back-scattered to 200 km altitude? The answer appears to be a qualified yes, depending on tradeoffs between laser pulse energy, repetition rate, range resolution, etc. The results are encouraging enough to warrant

a full-scale mission analysis specifying various orbits, percentage coverage of the atmosphere, and modes of operation which depend on cloud cover and the geographical regions of interest.

The present report describes how one arrives at a qualified yes answer and touches only briefly on equations of mission design. The main topics dealt with here are:

- What are the needs of the basic and applied atmospheric sciences as regards humidity data, both locally and globally? (Section 2)
- How are these needs met by conceivable lidar returns to the Space Shuttle, taking account of both atmospheric backscatter and H₂O absorption? (Section 3)
- What basis of confidence exists for sufficiently powerful, tunable and stable lasers that can be designed for the Space Shuttle within the bounds of present technology? (Section 4)

It will be seen that, taken together, the answers to these questions imply that the overall concept is sound and deserves further study -- not only from the viewpoint of mission design, but also demonstration of a breadboard system. The latter has indeed been undertaken under a follow-on grant (NSG-1156) for joint work between NASA-Langley and the University of Maryland. Thus the content of Sections 3 and 4 relates partly to feasible, near-term studies from low altitude as well as to Space Shuttle performance per se.

On the basis of the results reported in the following sections, we recommend that NASA undertake a mission definition study for Space Shuttle lidar measurements of atmospheric water vapor. For such a study the meteorological considerations of Section 2 will be paramount, and the

results of Sections 3 and 4 (and other, related studies by NASA-Langley) will be useful for scaling purposes.

We wish to acknowledge assistance from several sources. Professor W. Benedict (Institute for Molecular Physics, University of Maryland) provided new data on the H₂O spectrum and was available for many helpful discussions. Professor W. Zoller (Department of Chemistry, University of Maryland) gave valuable insight into polar applications. Dr. Adarsh Deepak (Old Dominion University and NASA-Langley) discussed approximations for aerosol scattering early in the project. Dr. Charles Bell (Naval Surface Weapons Center) provided timely assistance with a ruby laser that was used for preliminary experiments on dye laser pumping, and Mr. Barry Maki carried out these experiments.

Both the financial and scientific support of this project by the Lidar Applications Section at NASA-Langley have been invaluable. We wish to thank G. B. Northam, S. Poultney, E. Browell, F. Mills and L. Gordley for many discussions, criticisms and calculation that furthered our work.

The University of Maryland has supported this research through IFDAM, the Graduate Program in Meteorology, and both the Horn Point Laboratory and the Inland Environmental Laboratory of the Center for Environmental and Estuarine Studies. In particular the support by Professors H. E. Landsberg, P. E. Wagner and D. A. Pemberton is gratefully acknowledged.

2. A Summary of Meteorological Requirements for Water Vapor Data and Possible Space Shuttle Applications

2.1 Introductory Remarks

The water content of air affects much of our daily life. Obviously, what we call weather - rain, snow, sleet and hail are direct consequences of the water content of air. In addition, the human and animal discomfort indices and forest fire index require humidity observations as input variables. Industrial processes involving paper, paint, woodwork, textiles and precision instruments are very sensitive to the surrounding humidity. In agriculture, harvesting and storage of grains require low atmospheric humidity. Excessive humidity has the dual effects on plant growth of changing evaporation from plant surfaces and of encouraging disease (e.g., Bourke, 1955 and Wallin, 1967).

A considerable amount of information concerning the average seasonal, spatial and vertical distribution of the water vapor content of the troposphere and lower stratosphere has been obtained from standard meteorological surface and upper air networks and from special stratospheric studies (e.g., Mastenbrook, 1966). Excellent average tropospheric water vapor profiles for different seasons and geographical locations are given by McClatchey et al. (1970) and the U. S. Standard Atmosphere (1966) and by Mastenbrook (1971) for the lower stratosphere. Climatological maps of surface and column water vapor content are given in Selected Climatic Maps of the United States (1965). Little climatological data on water vapor is available over the oceans.

Unfortunately these climatological data are not applicable to important atmospheric problems due to the fact that on an individual

day, the water vapor density at a given tropospheric level may differ from the seasonal average by an order of magnitude, and the vertical variation is considerably different from day to day. This large variability is due to the fact that the water vapor distribution is a contributor to and a result of a given weather situation. That is, water vapor plays an important role in atmospheric processes at all time, and spatial scales of motion ranging from the molecular scale (i.e., evaporation) to the general circulation. Water vapor plays an important role in atmospheric energetics since it provides a source of energy through the release of latent heat, its presence affects the release of energy, it plays an important role in the radiation balance and, although a trace constituent in the stratosphere, it plays a role in stratospheric photochemistry.

Improved methods of measurement of water vapor alone will not lead to better theoretical models or weather forecasts. It is only through the simultaneous measurement of the thermodynamic and hydrodynamic properties of the atmosphere combined with advanced knowledge and mathematical modeling of the processes governing the interaction of the important variables that will result in improved forecasting.

In this section we:

1. Summarize the accuracy of water vapor measurement required by modelers and forecasters at a number of scales of motion.
2. Review current and planned direct and indirect methods for operational use in obtaining atmospheric water vapor data.
3. Identify important meteorological applications of water vapor data which might be obtained by a Space Shuttle Laboratory lidar system.

2.2 Water Vapor and Temperature Measurement Requirements

Desired measurement accuracies for atmospheric variables for many scales of atmospheric motion have been specified for different experiments associated with the Global Atmospheric Research Programme (GARP) (see, Döös, 1970). The measurement accuracy specification by different GARP committees does not encompass all possible scales of motion; however, they do cover the scales of motion which are possible to observe from the space shuttle.

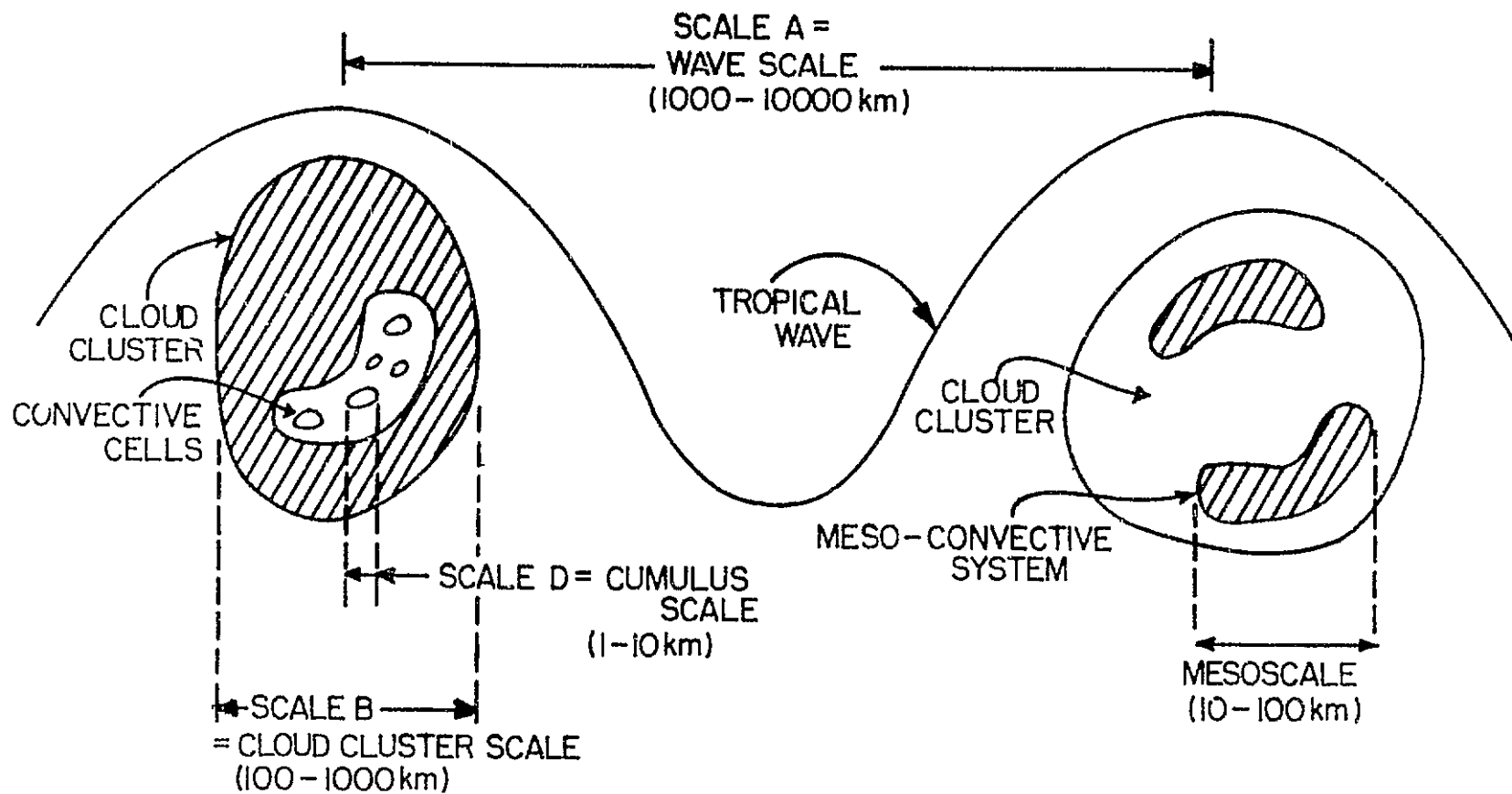
Fig. 1 is a diagram presented by Kuettner et. al. (1974) which illustrates the four major classifications of scales of atmospheric phenomena in the tropical atmosphere. Although the representation shown in Fig. 1 is only directly applicable to the tropics, the same scales of motion predominate in mid-and high latitudes.

The largest scale, the A-scale, incorporates the so-called synoptic and planetary scales. This scale is used for describing atmospheric waves of long lifetime, sometimes several weeks, and long wavelength. These waves include the so-called tropical easterly waves, Rossby-gravity waves of wavelength 5000 to 10000 km, and Kelvin waves.

The next smaller scale, the B-scale is the scale on which tropical "cloud clusters" develop. It is thought that they form the link between the short-lived smaller scale convective elements and the long-lived tropical waves and the Intertropical Convergence Zone (ITCZ). This scale of motion is generally not of great importance at higher latitudes (Kuettner et. al., 1974).

The C-scale refers to the scale of organized convection that form subsystems of the cloud clusters. In mid-latitudes, the term "mesoscale" is often used to denote this scale of phenomena. Two mid-latitude examples of mesoscale phenomena are squall lines and groups of severe thunderstorms.

Figure 1



The smallest scale shown in Fig. 1, the D-scale, contains the individual convective elements; therefore, it is sometimes called the cumulus scale. This is also the scale of important variations of meteorological variables within an urban area.

The accuracy and precision and time and spatial resolution of temperature and water vapor measurement necessary to satisfy the needs of forecasters and modelers of all meteorological processes at the scales of motion depicted in Fig. 1 have not been specified. However, the data requirements for some previous and planned GARP experiments have been cited in the literature. This section summarizes the data requirements for two such experiments for which the data requirements have been defined and which appear most stringent. These requirements should serve as a guide to the applications which might be made of data obtained from the Space Shuttle laboratory.

The data requirements necessary for forecasters and modelers of large scale atmospheric phenomena have been thoroughly discussed by Döös (1970) in conjunction with planning for the First GARP Global Experiment (FGGE) to be conducted in 1979-1980. The primary objective of FGGE is to provide initial and verifying conditions for experiments to enlarge predictability in the medium range (i.e., from a few days to a few weeks), and in the extended range (i.e., from a few weeks to a few months). A comprehensive discussion of the FGGE objectives is given by the GARP Joint Organizing Committee (1974).

The first major GARP experiment, the GARP Atlantic Tropical Experiment (GATE), was conducted during the period June through September (1974) (see Kuettnner et. al. (1974)). The GATE objective was to observe in sufficient detail the convective systems over the tropical Atlantic

Ocean, and to observe the larger scale atmospheric structure and motion systems in which the convective systems are embedded, so that the interaction between the phenomena on these different scales is determined. An understanding of this interaction is to be used to develop parameterization schemes for cumulus convection in large scale atmospheric models (Betts and Rodenhuis, 1974). The temperature and water vapor measurement requirements for the GATE Convection Subprogram at the cloud-cluster, meso-and cumulus scale were given by Betts and Rodenhuis (1974, pp. 59-63).

Table 1 summarizes the large scale FGGE and smaller scale GATE temperature and water vapor measurement requirements. It should be noted that Δt refers to the time separation between simultaneous observations at each data point, Δx refers to the horizontal distance between successive data points and Δz refers to the vertical separation of data required at each observation point. The accuracy requirements for temperature are in degrees Celcius and in percent relative humidity for water vapor. Appendix 1 discusses the relationship between relative humidity, water vapor mixing ratio, specific humidity and water vapor density. It should be noted that the stated accuracy requirements refer to relative accuracy.

It is quite apparent from Table 1 that as the scale of motion decreases, the required time, spatial and vertical resolution become smaller, and the accuracy requirements become more stringent. This is due to the fact that, in general, as the scale of phenomena become smaller, the shorter the lifetime, the more sensitive a model is to initial conditions (i.e., through finite differences), and the more rapidly observation errors propagate through a prediction scheme.

TABLE 1. TEMPERATURE AND MOISTURE OBSERVATIONAL REQUIREMENTS

SCALE	NETWORK SIZE	RESOLUTION			ACCURACY	
		Δt	Δx	Δz	TEMPERATURE	WATER VAPOR
<u>LARGE SCALE</u> 1000-10,000 KM	GLOBAL	12 HRS	500 KM	3 LEVELS IN THE LAYERS 1000-600, 400-200, 125-80MB TWO LAYERS IN THE TROPOSPHERE	0.5 + 1.0°C	10 TO 20%
<u>CLOUD-CLUSTER</u> 100-1000 KM	1000 X 1000KM	6 HRS	250	VARIABLE 50 TO 200M FROM 0 - 2 KM .5 - 3KM FROM 2 - 18 KM	0.2 TO 0.5	5%

TABLE 1. Continued

SCALE	NETWORK SIZE	RESOLUTION			ACCURACY	
		Δt	Δx	Δz	TEMPERATURE	WATER VAPOR
MESOSCALE 10-100 KM	50 x 50 TO 100x100KM	1.5 - 3 HRS	10 KM	VARIABLE HIGHEST RE- SOLUTION NEAR THE SURFACE OF ORDER 50-200M	0.2 ⁰ c	2 - 5%
CUMULUS SCALE 1 - 10 KM	10 x 10 KM	15 MIN	1 KM	VARIABLE HIGHEST RESOLU- TION NEAR THE SURFACE OF ORDER 20 TO 200 M	<0.2 ⁰ c	<2%

2.3 Current and Planned Operational Atmospheric Sounding Systems

The largest amount of regularly obtained atmospheric soundings of temperature, water vapor, and wind velocity come from radiosonde ascents from the worldwide network of upper air stations (see the Weather Station Index (1965) for a complete listing). These stations are irregularly spaced at roughly 400 to 500 km intervals in populated regions of the northern hemisphere but at much coarser intervals in South America, Africa and Asia. The oceanic regions are covered by very widely spaced ship stations.

Radiosondes are launched from each station at least twice daily at 0000 and 1200 GMT. Some stations also obtain data at 0600 and 1800 GMT. Temperature, water vapor and wind data are reported at a group of mandatory pressure levels at approximately 1.5 to 2.0 km intervals between the surface and 30 km. Data are also reported at intermediate levels if significant deviations from standard soundings occur. The list of mandatory levels and criteria for significant levels is given in the Manual for the Radiosonde Code (1963). It should be noted that the designs and characteristics of radiosondes are not standard; therefore, some difficulties may arise when interpolating data across international boundaries.

The radiosondes used by the United States military and National Weather Service (NWS) employ a thermistor and carbon strip hygistor for temperature and humidity measurement. The accuracy of these systems have undergone intensive review in recent years by Ostapoff et. al. (1970), Morrissey and Brousaides (1970), Teweles (1970), Lenhard (1970, 1973), Betts et. al. (1974), and Brousaides (1975). The work of

Lenhard (1973) gives an upper bound of ± 0.2 C for the NWS radiosonde temperature error. This is well within the accuracy requirements for the previously discussed scales of motion.

The accuracy of the NWS sonde humidity device is less certain. The work of Ostapoff et. al. (1970) showed a diurnal relative humidity (RH) variation of 20% RH due to improper ducting and radiation errors. This led to a new design of the NWS radiosonde case (Friedman, 1972).

For calibration purposes, the NWS requires a $\pm 5\%$ RH repeatability under all conditions except that below 30% RH, a $\pm 7\%$ RH error is allowed (Brousaides, 1975). Betts (1974) reports observed errors of $\pm 5\%$ RH at high RH values. However, Quiring (1973) and Brousaides (1975) show that errors much larger than $\pm 9\%$ RH occur when the humidity drops below 25%. As a result, the NWS no longer reports measured data less than 20% RH. In addition, relative humidity data are terminated when the temperature is less than -40°C .

To summarize, temperature and water vapor data from radiosonde ascents are of sufficient quality for studies at scales of motion ranging from the meso-to the synoptic scale. However, mesoscale studies require a denser network than is available. Furthermore, the radiosonde gives poor humidity data at low humidities, and stratospheric water vapor data are not obtained.

A large number of research and development and operational earth orbiting satellites, from which useful meteorological data may be obtained, have been launched or are in the planning stages. Table 2 summarizes the reported capabilities of instrumentation on board the research and development satellites Nimbus 5, launched December 1972, and Nimbus F, launched June 1975, and the latest of an operational

series, ITOS-G, launched November 1974. Each of these satellites is placed in a sun-synchronous polar orbit. A comprehensive list of capabilities of previous and planned meteorological satellites is given by the Compendium of Meteorological Satellites and Instrumentation (1973).

It appears that the present and planned remote sensing techniques are capable of providing water vapor data at the time and spatial resolution required for large scale atmospheric studies. In addition, at least one technique will provide data on stratospheric water vapor. However, none of the remote sensing techniques give data with sufficient resolution for application to mesoscale studies.

TABLE 2. Reported Capabilities of Meteorological Satellite Systems

Instrument	Range (km)	Resolution (km)		Accuracy	
		Δx	Δz	Temperature	Humidity
Nimbus 5-ITPR Infrared Temperature Profile Radiometer	0 to 25	30	3 to 5	2.0°C	
	0 to 6	30	6		20% RH
Nimbus 5-SCR Selective Chopper Radiometer	0 to 45	30	3 to 7	2.0°C	
	0 to 10	30	3		20% RH
Nimbus 5-NEMS Microwave Spectrometer	0 to 18	192 x 192	5	2.0°C	
	0 to 6	192 x 192	6		
Nimbus 5-THIR Temperature Humidity Infrared Radiometer	5 to 10	5	8	-	20% RH

TABLE 2. Continued

Instrument	Range (km)	Resolution (km)		Accuracy	
		Δx	Δz	Temperature	Humidity
ITOS-VTPR Vertical Temperature Profile Radiometer	0 to 30	50 x 50	3 to 5	1.0 to 2.0°C	
	0 to 10	50 x 50	5		20% RH
Nimbus F-HIRS High Resolution Sounder	0 to 45	30	2 to 7	2.0°C	
	0 to 12	30	4		20% RH
Nimbus F-PMR Pressure Modulated Radiometer	0 to 65	71 to 360	3 to 5	5.0°C absolute 2.0°C relative	-
Nimbus F-SCAMS Spectral Scanning Microwave Spectrometer					
Nimbus F-LRIR Limb Radiance Infrared Radiometer	14 to 75	400	2 to 3	3°C	
	14 to 50	400	2 to 3		mixing 20% ratio

2.4 Applications of Water Vapor Profiles Obtained from the Space Shuttle Lidar

The meteorological applications which might be made of water vapor profiles obtained with the Space Shuttle lidar system depend primarily upon:

1. the accuracy and precision of the lidar retrieval technique.
2. the horizontal and vertical resolution possible from Space Shuttle altitudes.
3. the inclination and duration of the Space Shuttle orbit.

In order to have application to all the scales of motion shown in Fig. 1, the retrieval technique must meet the requirements of the cumulus scale. If one uses the rough estimate of 10 km sec^{-1} for the ground speed of the shuttle, one would require a 100 hertz firing rate of the lidar system in conjunction with a mirror system in order to obtain one snapshot of the atmosphere at the horizontal resolution required at the cumulus scale. The power requirements for that firing rate appear to be beyond the present or near future state of the art. However, it appears that 10 hertz firing rate may be attainable for short durations by the time of Space Shuttle flights. Therefore, with a proper mirror system, the smallest scale the lidar might be applied to is the mesoscale. In addition, such a firing rate could provide vertical profiles at the horizontal resolution of the cumulus scale. Assuming the accuracy and vertical resolution requirements of Table 1 can be met, the Space Shuttle lidar can provide water vapor data with some applicability to all the scales of motion shown in Fig. 1.

The application of water vapor data to studies of large scale atmospheric processes depends primarily upon the inclination and duration of the orbit. Obviously, a low inclination orbit around the same latitude circle could provide, at best, a time series of data from data sparse

oceanic and unpopulated regions. On the other hand, a polar orbit would provide global coverage, although the data would be asynoptic in character since they would not be gathered at one time. However, four dimensional data assimilation techniques (e.g., Rutherford, 1972; Bengtsson and Gustavsson, 1972) would make proper use of these data. In either case, however, it appears that current or planned passive satellite retrieval techniques can provide water vapor data at the resolution required for large scale atmospheric studies.

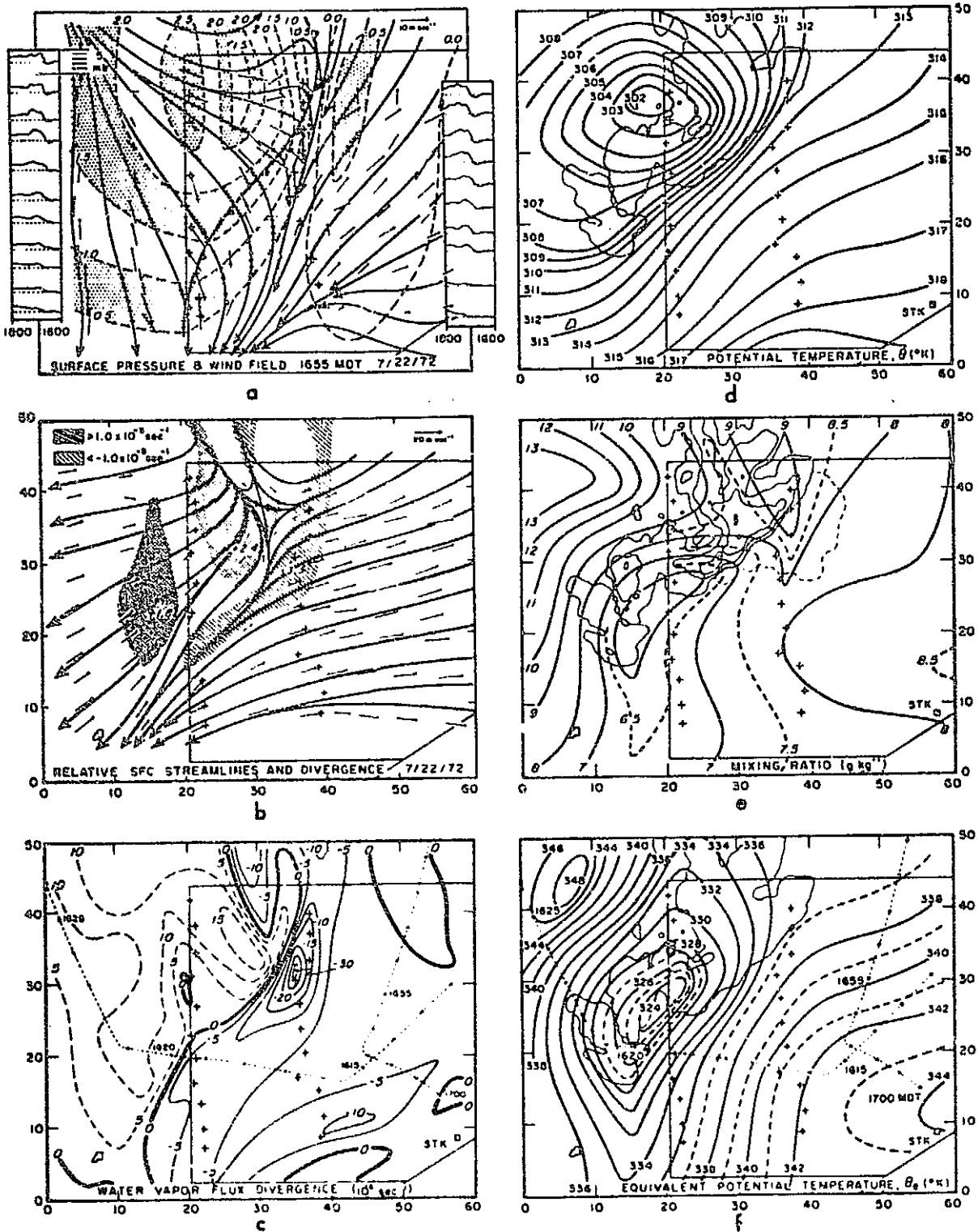
It appears that the greatest application of Space Shuttle lidar data would be to studies and modeling of phenomenon at the cloud-cluster and meso-scales. A number of such studies have been performed in recent years and several are planned for the future. These studies include GATE-1974 (cloud-cluster and mesoscale), the National Hail Research Experiment (NHRE) - 1971-76 (mesoscale) - Foote and Frankhauser (1973), the Air Mass Transformation Experiment (AMTEX) - 1974-75 (synoptic and mesoscale) - Lenschow and Agee (1974), the Severe Environmental Storms and Mesoscale Experiment (SESAME) 1978-80, see Lilly (1975), and the Polar Experiment (POLEX) - 1975-76, (synoptic-mesoscale), Weller and Bierly (1973).

These experiments require the simultaneous measurement of many atmospheric variables, including temperature and water vapor at meso-scale resolution over a limited area larger than the cloud-cluster scale. Fig. 2 shows the horizontal surface distribution of several meteorological parameters determined by Foote and Frankhauser (1973) in the vicinity of a mid-latitude mesoscale convective feature. This figure points out the complexity of the horizontal distribution of several important meteorological parameters and illustrates the necessity for measurements at

small horizontal spacing. It should be noted that a detailed three dimensional mapping of one parameter, such as the water vapor mixing ratio (Fig. 2(e)), is not sufficient to predict the location of the greatest water vapor convergence (Fig. 2(c)) or the time variation of a mesoscale convective feature. It is apparent that the usefulness of a Space Shuttle water vapor lidar to studies of mesoscale convection would be providing supplemental data to an existing field experiment.

An important meteorological feature, in which water vapor plays an important role, is the so-called "dryline" front. The dryline has been discussed in detail by Rhea (1966) and Schaefer (1974a, 1974b, 1974c). Briefly, the dryline is a narrow zone across which a sharp moisture gradient occurs (roughly a factor of two change in mixing ratio over 10 km). It often exists and moves under synoptically quiescent conditions; however, it is often associated with thunderstorm development over the southern plains. The dryline is oriented north-south, approximately parallels the terrain contours and is often found over west Texas and Oklahoma during the spring and early summer. The dryline surface has a characteristic steep profile, being roughly vertical to approximately 4000 ft. above its surface intercept. It then tilts rapidly eastward to become nearly a horizontal surface. Drylines typically move roughly 500 km eastward during the day and westward at night. Although narrow, the dryline may be over 500 km in length. According to Schaefer (1974c), the dryline is also a significant feature during the pre-monsoon months over India and Central West Africa.

Schaefer (1974a) has developed a numerical model of dryline movement. One large uncertainty in forecasting its position is its initial position. Currently, its position is obtainable only after it has passed



Surface meso-analyses at 1655 from data measured at stations located at stars and extrapolated east and west by time-space conversion. (a) Surface wind vectors, streamlines and isobars of perturbed pressure (mb). Actual pressure traces are shown on panels to left and right. Heavy barbed line shows position of gust front and "temperature break." (b) Relative wind vectors, streamlines and velocity divergence. Extremes are shown at their respective locations. (c) Water vapor flux divergence. (d) Potential temperature. (e) Mixing ratio with radar echo intensity contours at 1° elevation (solid) and echo "overhang" at 5° elevation (dashed), superimposed. (f) Equivalent potential temperature. Light dashed line with dots on (e) and (f) shows adjusted aircraft track and 1-min positions. The 25-dBZ echo contour is shown for reference on (d) and (f). Tick marks on outer boundary are at 10-km intervals.

Figure 2

REPRODUCIBILITY OF THE ORIGINAL PAGE IS POOR

one of the widely spaced surface stations. According to Schaefer (1974b), the temperature does not vary across the dryline. Therefore, the factor of two change in the mixing ratio across the dryline is due only to a variation in the water vapor density. If the Space Shuttle water vapor lidar could obtain the surface to 4000 ft column content with less than ten percent random error, observations at one to two kilometer horizontal resolution could be used to position and track the dryline front on each orbital pass.

A 10 hertz lidar sampling rate would allow a cross section of vertical water vapor profiles with roughly one kilometer horizontal resolution. Such data could be used to study the variation of water vapor in urban areas and urban effects on the larger scale water vapor field. Experiments of this kind would be useful in delineating areas conducive to fog and smog formation and downstream convective development.

A final application, which has not been studied in detail, is the determination of the stratospheric water vapor content. The only current passive instrument suited for this purpose is the Nimbus F Limb Radiance Infrared Radiometer (LRIR) which claims an accuracy of $\pm 20\%$ mixing ratio at 2 to 3 km vertical resolution for the 15 to 50 km range. In order to be competitive, the Space Shuttle water vapor lidar would require equal or better accuracy.

Perhaps the best method for obtaining stratospheric water vapor information from a Space Shuttle lidar would be the measurement of the backscatter from the tops of optically thick cirrus. If these observations could be compared to similar observations in clear areas, one might obtain estimates of the amount of water vapor injected into the stratosphere by

thunderstorms. However, it is likely that the clear column lidar observations would be dominated by tropospheric water vapor. Therefore, it would be extremely difficult to extract the injected amount with the lidar unless an independent observation were obtained. The applicability of a Space Shuttle water vapor lidar to this problem requires further simulation using estimates of the stratospheric aerosol distribution and the optical properties of cirrus clouds.

To summarize, Space Shuttle lidar determined water vapor profiles might be applied to:

1. augmenting synoptic observations in data sparse areas.
2. three-dimensional mapping of mesoscale water vapor fields.
3. detection and tracking of "dryline" fronts.
4. determination of urban influences on the larger scale water vapor field.

3. Lidar Simulation

This section estimates the feasibility of measuring atmospheric water vapor via orbital lidar. The calculation starts with laser radar equations representing backscatter with and without molecular line absorption; the magnitudes of off-line backscatter are demonstrated (3.1). Extensive prior data on water line strengths are summarized in 3.2 to indicate the available sensitivity to water vapor concentration. The wavelength range of greatest interest is $7000 \text{ \AA} - 1.0\mu$. This range is accessible to various tunable dye laser techniques, such as ruby laser pumping of polymethine dye solutions in a well-designed, narrow band cavity (see Section 4).

Several lidar situations are then considered (3.3) starting with uniform and perturbed atmospheres at 0, 3, 10 and 20 km (stratosphere) altitudes. These simulations are indicative of results to be obtained in "ground truth" measurements (ground-based and airborne). An approximate treatment of polar observations is also given. Finally, vertical atmospheric soundings from orbit and from ground stations are calculated. Errors are discussed (3.4) as regards their propagation through the lidar equation to render the measured water vapor concentration imprecise; conclusions are given as to required laser energy and feasible altitude resolution.

3.1 Preliminaries

We adopt a monochromatic lidar equation for the ratio $R = N_{\text{rcd}}/N_{\text{trans}}$ between the received and transmitted numbers of photons in the laser pulses:

$$R = K \left\{ \frac{cT}{2} \cdot \beta_{\pi}(r) \cdot \frac{A}{r^2} \right\} e^{-2 \int_0^r \beta_t(r') dr'} , \quad (1)$$

where K is a total optical system efficiency, τ is the "range gate" or open time for accumulating N_{rcd} , β_{π} is the volume coefficient of backscatter and is in general a function of the lidar range r , and A/r^2 is the element of solid angle subtended by the receiving telescope of area A . Since $c\tau/2$ is the range resolution (km), and the dimensions of β_{π} and A/r^2 are respectively $(\text{km-sterad})^{-1}$ and $(\text{sterad})^{+1}$, the expression in brackets is dimensionless.

The last term represents all extinction processes during two-way passage of the beam along the line of sight. The total extinction per unit length can be decomposed into absorption and scattering by molecules and particles:

$$\beta_T = \beta_{a,m} + \beta_{a,p} + \beta_{s,m} + \beta_{s,p} \quad (2)$$

$$\stackrel{d}{=} \beta_{a,m} + \text{III (all in units km}^{-1}\text{)}.$$

Molecular absorption is singled out for attention because it is usually much more dependent on wavelength than the other three terms (III). Explicit use of this property is made below in setting up the simplest form of the differential absorption method.

The lidar equation (1) assumes no refractive or multiple scattering effects in the atmosphere; also the detector must be so apertured and gated that at each range it receives all the light, and only the light, backscattered from that conical slice through the atmosphere which is illuminated by the slightly divergent laser beam.

Scattering processes therefore enter twice into equation (1); they

ultimately determine the 180° backscatter coefficient β_π and give rise to part of the extinction via $\beta_{s,m}$ and $\beta_{s,p}$. To simplify calculations, we will let

$$\beta_\pi = \sum_i \frac{\epsilon_i}{4\pi} \beta_{si} \quad , \quad (3)$$

where $\epsilon = 1$ for molecules and small aerosols and $\epsilon = 0.2$ for large aerosols (Mie scattering). The latter reflects the fact that roughly 80% of the intensity of Mie scattering lies in the forward direction, leaving 20% for distribution over all angles. We assume that the rich fine structure of Mie scattering is usually washed out by distributions of particle size and composition found in nature.

Since these scattering coefficients and the particulate absorption $\beta_{a,p}$ are only weakly varying functions of the wavelength, we can set them equal in two lidar equations for closely spaced wavelengths (λ_0, λ) over which molecular absorption may vary drastically. λ_0 might be at the center of an H_2O line, for example, while λ might be 3 or 10 half-widths away. Since $|\lambda_0 - \lambda|$ can therefore be as small as $1-2 \text{ \AA}$, e.g. for H_2O and O_2 lines in the near infrared, it is reasonable to focus attention on $\beta_{a,m}(\lambda)$ and allow constancy of the other extinction coefficients over $\{\lambda_0, \lambda\}$.

The ratio of the lidar equations for the two wavelengths is then

$$Q(r) = R_\lambda(r)/R_{\lambda_0}(r) = \exp 2 \int_0^r (\beta_{a,m,\lambda_0}(r') - \beta_{a,m,\lambda}(r')) dr' \quad , \quad (4)$$

and $(1/Q)(d/dr)(Q)$ yields

$$\frac{d}{dr} [\ln Q(r)] = 2 [\beta_{\lambda_0}(r) - \beta_{\lambda}(r)] . \quad (5)$$

In general the molecular extinction will be $\beta = n(r) \sigma(r)$, where both the number density and the absorption cross section may vary along the line of sight. For sufficiently constant temperature and total pressure, changes in molecular line shape may be ignored, $\beta(r) = \sigma(\text{const.}) n(r)$, and

$$n(r) = \frac{\frac{d}{dr} [\ln Q(r)]}{2[\sigma(\lambda_0) - \sigma(\lambda)]} . \quad (6)$$

This is the central equation of the differential absorption method* whereby one obtains range-resolved $n(r)$ from the observed time (i.e., distance) behavior of the ratio Q between off-line and on-line lidar returns (Measures and Pilon (1972), Ahmed (1973), Byer and Garbuny (1973)).

For best results the normalized off-line return $R_{\lambda}(r)$ should be as large as possible, so that modest amounts of absorption in the on-line return are discernible with good statistical reliability. Essentially one is relying on atmospheric backscatter as a "distributed mirror" along the line of sight in order to get sufficient photons returned from any given layer without overly attenuating the beam for layers further away.

For a given range, the atmospheric scattering conditions β_s giving the optimum off-line return from that range can be calculated from equations (1) - (3). Since $\beta_{s,m}$ and $\beta_{s,p}$ vary with wavelength over intervals of hundreds and thousands of Angstroms, the optimal lidar wavelength for a given range will also depend on atmospheric conditions. Representative values of β_s are given in Table 3 which is taken largely from McClatchey et al (1972).

*Note added in proof: References to R. M. Schotland's pioneering and continuing work (1966, 1974) were inadvertently omitted. They are given on p. 86.

The principle of optimum β for a given range can be illustrated by assuming a uniform atmosphere in which one type of scattering is dominant. Then equation (1) can be written

$$R = C \frac{\beta_s}{r^2} e^{-2\beta_s r} \quad (7)$$

whence $\left. \frac{\partial R}{\partial \beta} \right|_r = 0$ yields $1 - 2r\beta = 0$, or

$$\beta_{s \max} = \frac{1}{2r} ; \quad (8)$$

e.g. to observe optimum lidar returns from 5 km, one should choose conditions such that $\beta_s = 0.1 \text{ km}^{-1}$; then also the return from 4 km will increase with increasing haziness while that from 6 km range will decrease.

These considerations are important in the design of ground-based experiments where the weather conditions are variable and where one would try to validate system errors prior to flying a system in an aircraft or satellite. Remsberg et al (1975) have recently reported estimates of the limits of utility of orbital, differential absorption lidars based on similar considerations of the off-line lidar return.

To illustrate the lidar returns for various situations, we plot in Figure 3 the off-line returns for four wavelengths and two uniform atmosphere situations according to McClatchey's (1972) summary of data on typical conditions. The lidar parameters are given in the figure. The curves were calculated according to equations (1) - (3). As to the absolute numbers of detected photons, it is noteworthy that the assumed 15 meter range resolution (30 nsec range gate) could well be increased

Table 3. Coefficients (km^{-1}) for Optical Extinction*
by Scattering in the Near Infrared ($\lambda=8600 \text{ \AA}$).

Model**	β_s , molec.	β_s , particle	$\beta_{\text{tot}} = \beta_{s,m} + \beta_{s,p}$
Hazy, midlatitude summer (sea level)	0.00193	0.440	0.442
Clear, midlatitude summer (sea level)	0.00193	0.0903	0.0922
Antarctic*** summer (3km ground level)	0.00145	0.00480	0.00625
Clear, midlatitude summer (alt. 3km)	0.00143	0.00817	0.00960
Clear, tropical (alt. 10km)	0.000677	0.00179	0.00247
Tropical (alt. 20km)	0.000154	0.000860	0.00101

* $\frac{dI}{dx} = \beta$; $\beta = \sigma n$

** Most data interpolated from tables given in "Optical Properties of the Atmosphere", R. A. McClatchey, R. W. Fenn, J. E. A. Selbv, F. E. Volz, and J. S. Garing, AFCRL Report no. 72-0497, (August, 1972).

*** Molecular scattering estimated as comparable to Subarctic summer (**); Particulate scattering based on $N = 150/\text{cm}^3$ (W. Zoller, private communication) and $\bar{\sigma}_p = 3.2 \times 10^{-10} \text{ cm}^2$ estimated from AFCRL** values for $\beta_{s,p}$ vs N .

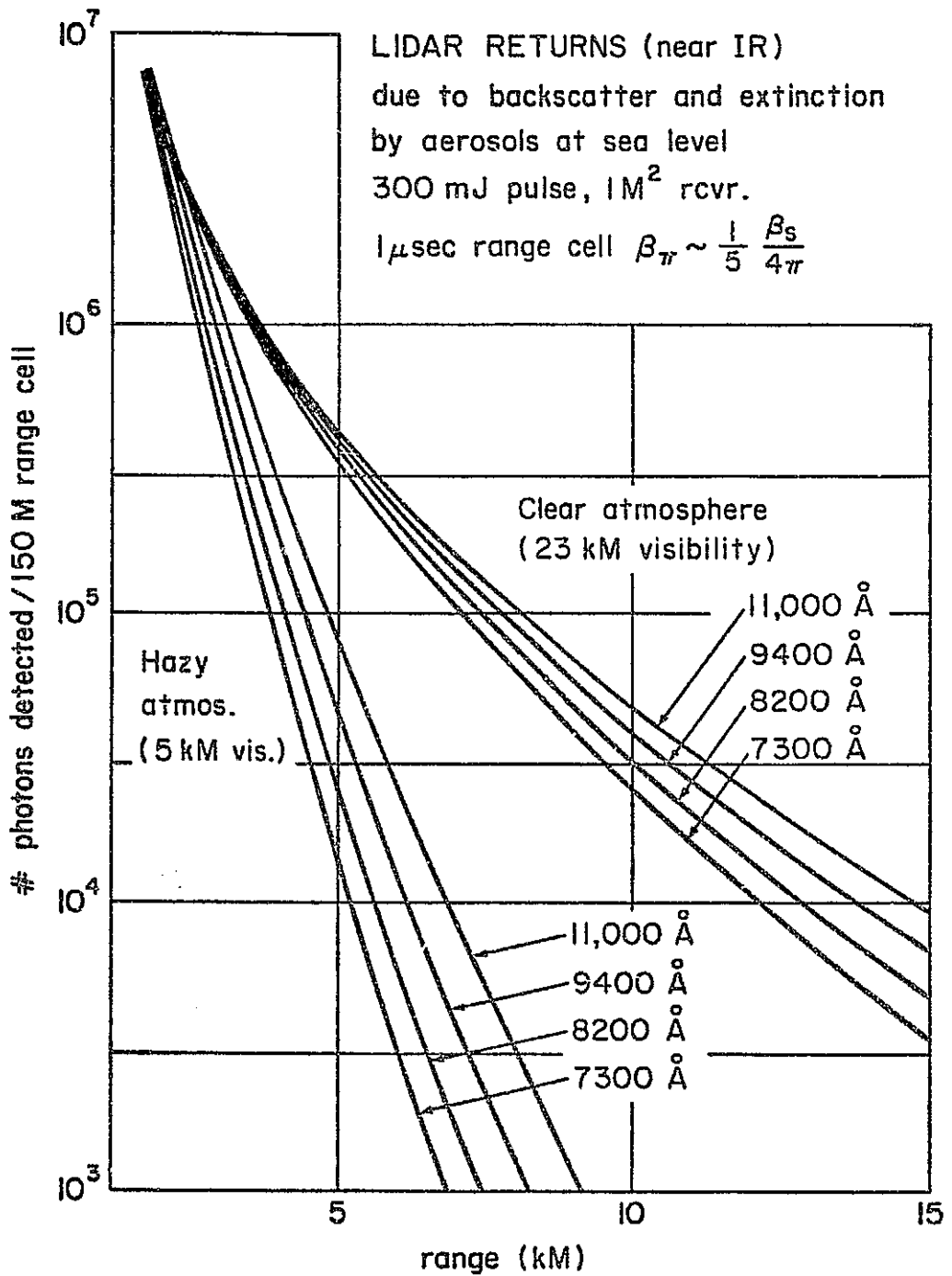


Figure 3

for larger scale observations at the longer ranges so as to minimize photon noise; also much smaller range resolutions, say 1M corresponding to the 6 nsec duration of a N_2 -laser-pumped dye, could be used out to ranges of a few km without incurring too great a photon noise. More examples of off-line lidar returns will be shown below as part of the discussion of the detectability of water vapor.

A further conclusion we make from Figure 3 is that the variation between models (for this λ -range) is much greater than the dependence on wavelength within a given model. Henceforth for any given aerosol model we will employ a standard calculating wavelength of 8600 Å to represent scattering in an average way for all H_2O lines between 7200 Å and 1.0 μ .

This facilitates a "parametric" view in which one assumes with reasonable justification that more-or-less constant tunable laser performance, detector efficiency, and atmospheric backscatter (for a given aerosol) can be obtained over this near infrared region -- and that the principal difference from case to case will reside in the H_2O absorption cross sections ("line strengths") available in any given band, and in the abundance of water vapor and aerosols in the atmosphere.

3.2 Water Spectrum: Wavelengths, Strengths and Widths.

This section arrives at useful representations of the strengths of water lines available in the visible and near infrared. Cross sections are indicated for the subset of lines we will call "temperature insensitive" -- namely those lines whose lower state populations are stationary with temperature for temperatures in the vicinity of 300°K. This will guarantee that the cross sections are representative of the values to be employed in atmospheric observations, since temperature-insensitivity will be an important property of any procedure for determining molecular abundance.

The extent of the H₂O absorption spectrum into the visible is indicated in Fig. 4, which is a low resolution scan of atmospheric transmission (sea level) over a 300 M path. Tunable dye laser techniques enable wavelengths up to 1.1 μ to be used for absorption measurements, and the parametric oscillator technique works well beyond this wavelength. What concerns us then is the strength of lines in the various bands such as at 7200 Å, 8300 Å and 9400 Å. We will see that many of these lines are sufficiently strong for [H₂O] assay from orbit and from the ground, while the 1.4, 1.9, 2.7μ, ... bands are too strong unless one is concerned with stratospheric H₂O. The lines near 5900 Å are interesting because of their coincidence with the region of peak performance by dye lasers (Rhodamine 6-G), but fall on the weak side as regards general applicability to atmospheric problems.

To illustrate the orders of magnitude involved, recent measurements by Meredith et al (1973) at Science Applications Inc. yield peak cross

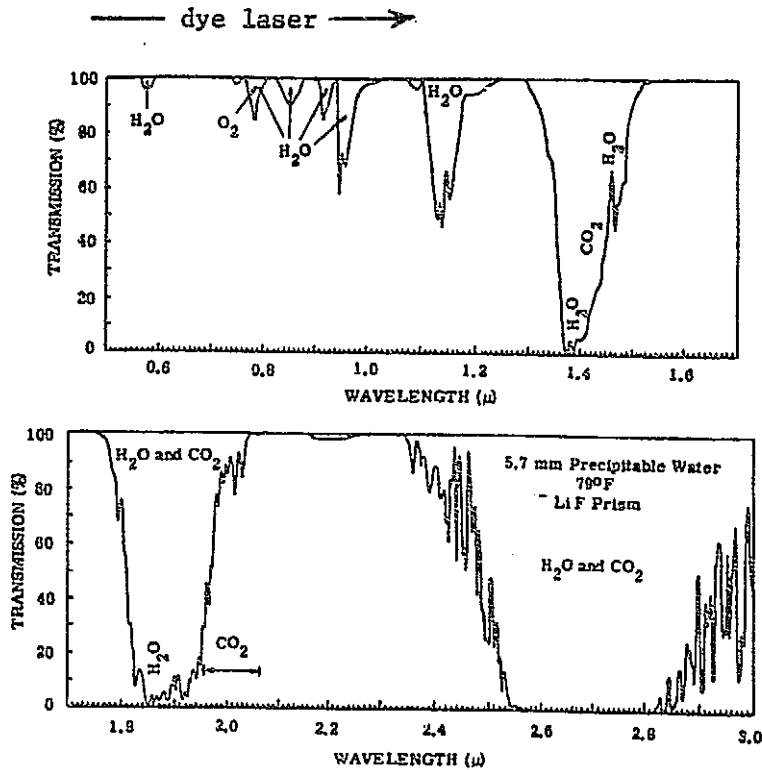


Figure 4. Atmospheric transmission over a 300 M path, 0.5-3.0μ [taken from Handbook of Military Infrared Technology (Ed. W. L. Wolfe) Office of Naval Research and U. S. Govt. Printing Office (1965); original source: H. W. Yates and J. H. Taylor, "Infrared Transmission of the Atmosphere", NRL Report 5453, ASTIA AD 240188 (1960).]

REPRODUCIBILITY OF THE ORIGINAL PAGE IS POOR

sections of order $4 \times 10^{-22} \text{ cm}^2$ for strong, temperature insensitive lines of H_2O near 9400 \AA . Thus the $1/e$ attenuation length (optical depth unity) for a laser tuned to such line centers is of order 100 M under typical ambient conditions of humidity ($\sim 2.7 \times 10^{17} / \text{cm}^3$, or $p(\text{H}_2\text{O}) = 10^{-2}$ atmos.). For atmospheric ranging over total path lengths of 10 km, such lines will clearly be of greatest interest in the polar regions where the absolute humidity is of order 1/100 of the above. For work in the temperate and tropical zones, one needs H_2O cross sections in the range $2 \times 10^{-24} - 2 \times 10^{-23} \text{ cm}^2$. Indeed these are to be found in the shorter wavelength groupings shown in Figure 4.

For quantitative discussion we will adopt the standard, semi-empirical relationship between absorption per particle in the line of sight and the strength and width of a Lorentzian line:

$$\sigma(\nu) = \frac{1}{\pi} \frac{S\gamma}{\{(\nu-\nu_0)^2 + \gamma^2\}} \quad (9)$$

σ is an absorption cross section (cm^2); $S = \int \sigma(\nu) d\nu$ is the line strength ($\text{cm}^2 \text{ cm}^{-1}$); γ is the line half-halfwidth (cm^{-1}). For absorption in a uniform gas of length l , the extinction of intensity $I(\nu)$ is given by

$$I(\nu)/I_0(\nu) = e^{-\beta(\nu)} = e^{-\sigma(\nu)n l} \quad (10)$$

where n is the total number density of the species in question (not the number in a given state). In this representation, the line strength S clearly involves the Boltzmann factor for the lower level of the line as

well as the partition function for the species. S is sometimes specified in units $(\text{cm}^{-1} / \frac{\text{gm}}{\text{cm}^2})$ in applications where one knows the mass density ρ and the total mass per unit area (ρL) in the line of sight.

In a previous report Wilkerson, Ercoli and Tomkins (1974) gave "detectabilities" for H_2O in terms of total gm/cm^2 , by requiring an optical depth $\beta(\nu) = 0.03$ and dividing by typical strong line strengths in various wavelength regions. The present summary of cross sections is more quantitative since it is based largely on new data which are extensive enough that the question of temperature-insensitivity can be addressed explicitly. We are greatly indebted to Professor W. S. Benedict (University of Maryland) and Dr. J. W. Brault (Kitt Peak Obs.) for the opportunity of using these data. Other published sources are also used for selected longer wavelength lines.

All the lines comprising the H_2O bands in the upper part of Figure 4 involve transitions to high vibrational states $\{v_1, v_2, v_3\}$ of the electronic ground state of H_2O ; e.g. $\{401\}$ near 5900 \AA , $\{301\}$ near 7200 \AA , and $\{211\}$ near 8200 \AA . What is of greatest interest from the standpoint of applications is the subset of lines within each band which originate on rotational sublevels whose populations n_R are temperature-stationary; i.e.,

$$\frac{\partial n_R}{\partial T} = 0 . \quad (11)$$

Restricting one's attention to these lines, and requiring that they be easily resolvable from all other lines in the H_2O spectrum, guarantees that one's lidar feasibility estimates will be based entirely on useful absorption lines.

Table 4 shows rotational levels for {o, o, o} and other vibrational states of H₂O, taken from Swensson et al (1970). The levels singled out are those for which the energy is about 300 cm⁻¹ above the rotational ground state. In descending order, these may also be written in (J'', K_a'', K_c'') notation as 3₃₀, 3₃₁, 4₁₃, 4₂₃, 4₂₂, 5₀₅, and 5₁₅, where J is the total angular momentum and K_a, K_c are the components relative to the axes of least and greatest moments of inertia of the H₂O molecule.

The indicated levels have nearly stationary populations, relative to T, for T = 300°K. This arises from the dominant T^{3/2} dependence in the H₂O rotational partition function Z_R(T) and the level population in each lower rotational level

$$n_{J'', K_a'', K_c''} \propto \frac{ne^{-E''/\theta}}{Z_R(0)} \quad , \quad (12)$$

where n is the total number density of H₂O molecules, E'' is the rotational energy (cm⁻¹), and we have introduced the corresponding temperature scale (cm⁻¹ units) $\theta = kT/hc$. Equations (11) and (12) yield the level-energy of maximum population

$$E''_{\max} = \frac{3}{2} \theta \quad ;$$

i.e., levels having $E'' \sim 310 \text{ cm}^{-1}$ will have stationary populations for T = 300°K. Thus the seven levels indicated in Table 4 are the most suitable* for temperature-insensitive determinations of H₂O abundance by means of

* F. Mills (NASA-Langley) has pointed out that lower levels (200-225cm⁻¹ in J = 3,4) may be better, if the laser line can be made very narrow compared to absorption lines, owing to the $\nu T^{1/2}$ dependence of the line width γ which offsets part of the T^{3/2} dependence in the molecular rotational partition function.

Table 4 [taken from The Solar Spectrum from $\lambda 7498$ to $\lambda 12016$ by J. W. Swensson, W. S. Benedict, L. Delbouille and G. Roland, Institut d'Astrophysique de l'Universite de Liege (1970).] Levels near 300 cm^{-1} are indicated, having $\partial n_r / \partial T \approx 0$ for $T=300^\circ\text{K}$.

H_2O Energy Levels (cm^{-1})

Note: Levels fully confirmed by combination differences are given to 0.01 cm^{-1} . Unconfirmed levels of high probability are given to 0.1 cm^{-1} , with the more doubtful indicated by †. Levels in different vibrational states whose properties are mixed by perturbation to an exceptional degree are denoted by *.

Section 1

J	τ	000	130	031	210	111	012
0	0	0.00	8273.95	8373.82	8761.57	8807.00	9000.13
1	-1	23.79	8297.34	8397.45	8784.60	8830.21	9023.47
	0	37.13	8323.31	8421.18	8799.65	8844.47	9037.21
	1	42.37	8329.38	8427.34	8805.14	8850.06	9042.81
2	-2	70.08	8343.14	8443.63	8829.48	8875.30	9068.76
	-1	79.48	8364.05	8462.44	8840.27	8885.19	9078.20
	0	95.17	8382.21	8480.80	8856.75	8903.46 *	9095.16
	1	134.91	8458.93	8549.96	8899.83 *	8944.67	9135.84
	2	136.17	8457.78	8550.99	8902.59	8945.98	9137.25
3	-3	136.77	8409.56	8510.34	8894.00	8939.93	9133.59
	-2	142.28	8424.59	8523.08	8900.65	8945.64	9139.04
	-1	173.36	8460.77	8560.12	8933.19	8979.65	9172.49
	0	203.30	8527.32	8620.92	8969.72	9013.98	9205.96
	1	212.15	8532.08	8625.98	8976.57	9020.17	9212.45
	2	285.23	8660.62	8746.52	9057.78	9098.39	9287.18
	3	285.43	8660.71	8746.64	9057.88	9098.61	9287.44
4	-4	222.06	8494.67	8595.54	8976.29	9022.30	9216.13
	-3	224.83	8504.35	8603.50	8979.63	9025.15	9218.84
	-2	275.52	8563.87	8664.07	9032.99	9079.71	9273.25
	-1	300.35	8620.23	8714.59	9061.13	9105.42	9298.21
	0	315.79	8633.10	8728.45	9077.32	9121.49	9315.17
	1	382.52	8758.52	8843.23	9152.59	9193.15	9383.09
	2	383.85	8757.11	8844.03	9153.62	9194.53	9384.67
	3	488.10	8929.44	9006.55	9267.95	9305.46	9490.94
4	488.13	8929.45	9006.58	9267.98	9305.48	9490.97	
5	-5	325.35	8598.88	8697.99	9075.60	9121.72	9316.16 *
	-4	326.64	8602.77	8702.45	9077.16	9123.01	9317.03
	-3	399.40	8690.08	8791.02	9154.15	9200.05	9304.90
	-2	416.22	8735.05	8830.14	9173.37	9218.02	9411.64
	-1	440.50	8761.65	8858.60	9204.67	9249.25 *	9444.68
	0	504.00	8876.35	8964.04	9289.06	9310.98 *	9502.71
	1	508.81	8878.58	8967.16	9275.03	9316.39	9508.21
	2	610.12	9050.92	9127.05	9380.7	9424.37	9611.51
	3	610.35	9051.02	9128.00	9388.95	9424.54	9611.79
	4	742.10	9257.35 †	9324.00	9528.51	9563.97	9745.18
	5	742.10	9257.18	9324.13	9528.51	9563.97	9745.18

QUALITY OF THE
IS POOR

optical absorption.

Lines originating on these levels are to be found in all the vibration-rotation bands shown in Figure 4. We culled available data on line strengths S and halfwidths γ within these bands, to establish reasonable limits on the absorption cross sections for temperature-insensitive lines in each wavelength region. The so-derived limits on σ as a parameter were then employed in lidar simulations. The remainder of this section deals with the line strength results.

9400 Å : {201}, {300}

The results of Meredith *et al* (1973) may be summarized by an absorption cross section $\sigma_o = S/\pi\gamma$ in the range $1.5 - 6.5 \times 10^{-22} \text{ cm}^2$ for several prominent lines which are temperature-insensitive or nearly so.

8200 Å : principally {211}

Farmer's (1971) study of the stronger lines in this region gave strengths in the range $(0.6 - 2.5) \times 10^{-23} \text{ cm}^{-1} / \frac{\text{molec.}}{\text{cm}^2}$ for seven temperature-insensitive lines. Assuming a common FWHM = $2\gamma = 0.16 \text{ cm}^{-1}$ for an STP atmosphere, one obtains $\sigma_o = S/\pi\gamma$ in the range $(2.5 - 10) \times 10^{-23} \text{ cm}^2$ for typical strong lines that would be employed for lidar measurements. Much smaller cross sections are also to be found in any such region, as can readily be judged from the large spread of H₂O absorption intensities seen in the Fraunhofer spectrum.

6810 - 7470 Å : {301, 103, 221, 202, 400, 023, 004, 122, 141, 320}

The range of line strengths for 90/100 temperature-insensitive lines terminating in these upper vibrational states can be adequately represented by $S = 3 \times 10^{-26} - 1.7 \times 10^{-23} \text{ cm}^{-1} / \frac{\text{molec.}}{\text{cm}^2}$, according to the data of Brault and Benedict. Their listing covers roughly 2250 lines in this region, clustered mainly in $\lambda\lambda$ 7000-7300. For $\gamma_{\text{STP}} \sim 0.09 \text{ cm}^{-1}$, the corresponding range of peak absorption cross section is:

$$\left\{ \begin{array}{l} \sigma_0 = 1 \times 10^{-25} - 6 \times 10^{-23} \text{ cm}^2, \\ \text{for } \lambda\lambda \text{ 6810-7470 (H}_2\text{O)} \end{array} \right. \quad (13)$$

Thus the strongest cross sections compare with those given above for the 8200 Å region. The magnitudes of the cross sections are distributed fairly evenly over this range, so that the factor-of-500 is reasonable to employ as a parametric variation of σ_0 in lidar calculations.*

6270-6660 Å : {231, 212, 311, 113, 410}

Data on about 1000 H₂O lines in this region were provided by Brault and Benedict. Of these, 55 are useful lines originating on levels whose

* The water line at γ 6943.8060 is well known for its proximity to the ruby laser emission. The two can be made to coincide by temperature-tuning the ruby, so that this line is a natural candidate for lidar measurements of H₂O. The line strength is given as $0.1773 \text{ cm}^{-1}/(\text{gm}/\text{cm}^2)$ by Brault and Benedict. Moreover the line arises from absorption out of the 4_{14} level of $\{0,0,0\}$, designated in Table II as $J=4, \tau=-3, E=224.83 \text{ cm}^{-1}$. In Mills' interpretation alluded to above, this line would show a temperature-insensitive central absorptivity for laser radiation having a linewidth $\ll 0.1 \text{ cm}^{-1}$. This leads us to provide an estimated effective cross section $\sigma = S/\pi\gamma$ here for the sake of completeness: $\lambda = 6943.8060 \text{ Å}; S = 5.31 \times 10^{-24} \text{ cm}^{-1}/(\text{molec.}/\text{cm}^2); \gamma_{\text{STP}} = 0.098 \text{ cm}^{-1}; \sigma_0 = 1.74 \times 10^{-23} \text{ cm}^2$. One obtains an optical depth $\beta = n\sigma_0 l = 1$ for $l = 2.1 \text{ km}$ and $n = 2.7 \times 10^{17} \text{ cm}^{-3}$ (typical 1% absolute humidity).

populations are temperature-insensitive; moreover, 50/55 have strengths in the range $1.5 \times 10^{-26} - 1.8 \times 10^{-24} \text{ cm}^{-1} / \frac{\text{molecule}}{\text{cm}^2}$. For $\gamma_{\text{STP}} = 0.08 \text{ cm}^{-1}$, one obtains

$$\begin{cases} \sigma_0 = 6 \times 10^{-26} - 7.2 \times 10^{-24} \text{ cm}^2 \\ \text{for } \lambda\lambda \text{ 6270 - 6660;} \end{cases} \quad (14)$$

i.e., the stronger lines here have cross sections which are about an order of magnitude lower than for the strong lines around 7200 and 8200 Å.

Summary (3.2)

For the near infrared below 1 micron wavelength, the effective absorption cross sections for H₂O lie mainly in the range $6 \times 10^{-26} \text{ cm}^2$ to $6 \times 10^{-22} \text{ cm}^2$, considering only the temperature-insensitive levels. For many of the calculations below, the parametric range for σ_0 was chosen to be $10^{-24} - 10^{-21} \text{ cm}^2$, since weaker lines are not useful and stronger H₂O lines are not to be found in this spectral region.

3.3 Results of Lidar Calculations

This subsection presents the results of lidar calculations for a variety of atmospheric situations:

- 3.3.1 Horizontal ranging at various altitudes in atmospheres of uniform composition (including stratospheric and polar cases of low aerosol and water abundance),
- 3.3.2 Detection of humidity variations via horizontal ranging,
- 3.3.3 Upward ranging by means of ground-based lidars,
- 3.3.4 Downward ranging from the 200km Space Shuttle altitude.

These cases are presented not only to discuss the feasibility of Space Shuttle observations per se, but also to show the nature of lidar returns - and their sensitivity to water vapor concentration - in experiments that will naturally be undertaken in the development of a Shuttle lidar capability.

3.3.1 Uniform Atmospheres (horizontal ranging)

Figures 5 and 6 depict the lidar returns at sea level for two of the standard atmospheres adopted by McClatchey et al (1972). Laser energy and range resolution are shown on the graphs; detection efficiency is assumed to be 10%. As mentioned earlier, the off line returns employ a wavelength of 8600 \AA which is reasonably representative of operation throughout the very near infrared ($7000 \text{ \AA} - 1\mu$). The terms "clear" and "hazy" refer to standard haze models, whose visibilities are 23 and 5 km and whose sea level aerosol densities are 2.828×10^3 and $1.378 \times 10^4 \text{ cm}^{-3}$, respectively. Water vapor concentrations were calculated at various altitudes by R. G. Ellingson. The "tropical" and "midlatitude summer" values for $[\text{H}_2\text{O}]$ at sea level are 6.405×10^{17} and $4.719 \times 10^{17} \text{ cm}^{-3}$, respectively. These models are employed in most of the calculations given here, except for special polar or stratospheric cases. Aerosols are usually treated as Mie scatterers having a backscatter coefficient $\beta_{\pi} \sim \frac{1}{5} \frac{\beta_s}{4\pi}$. Molecules are assumed to be Rayleigh scatterers and non-absorbing (except for H_2O).

The figures show both the off line signals and the returns as modified by on line operation with different H_2O absorption cross sections. The ranges of $\sigma_{\text{abs}}(\text{H}_2\text{O})$ have been chosen to represent the line strengths available in the very near infrared. The clear, tropical situation offers advantages for ground truth experiments, in that the aerosol extinction with range is far less drastic, and the higher humidity lends a greater accuracy

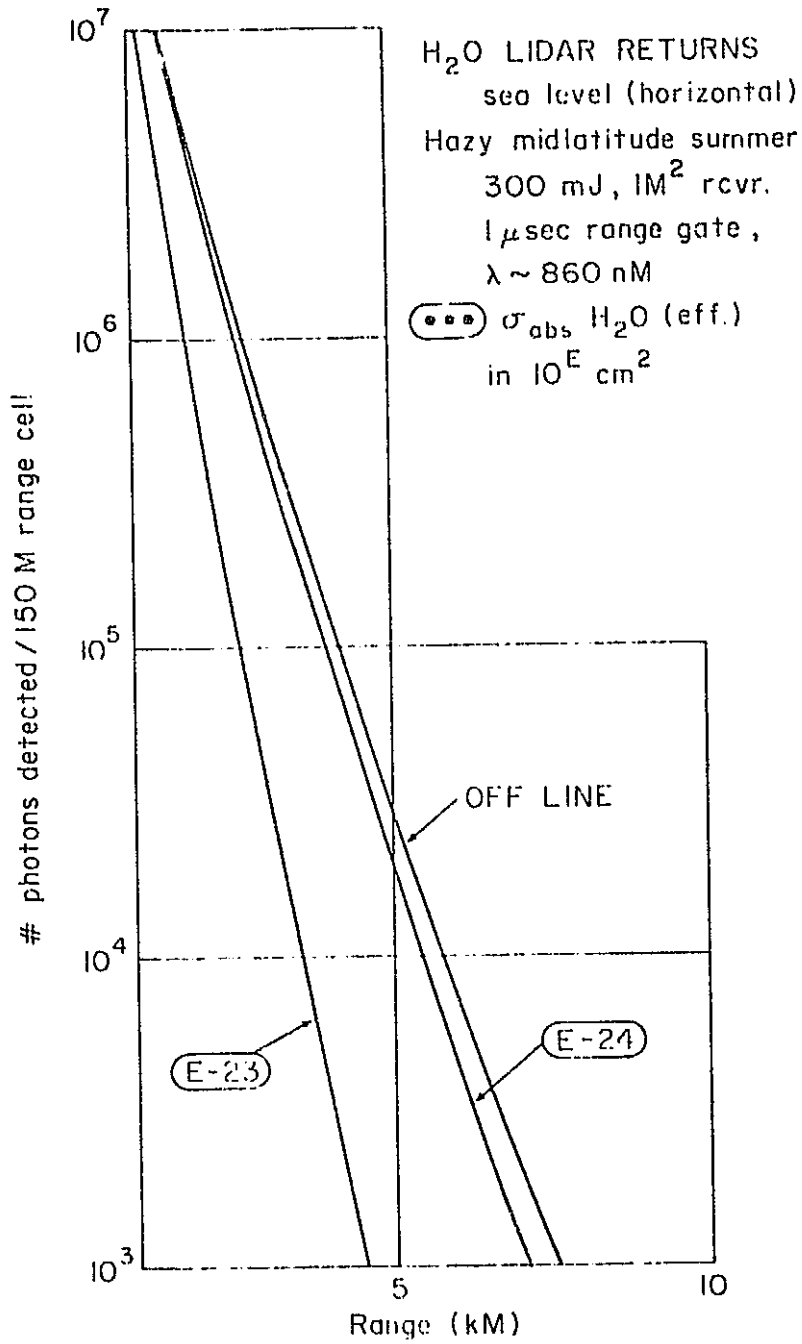


Figure 5

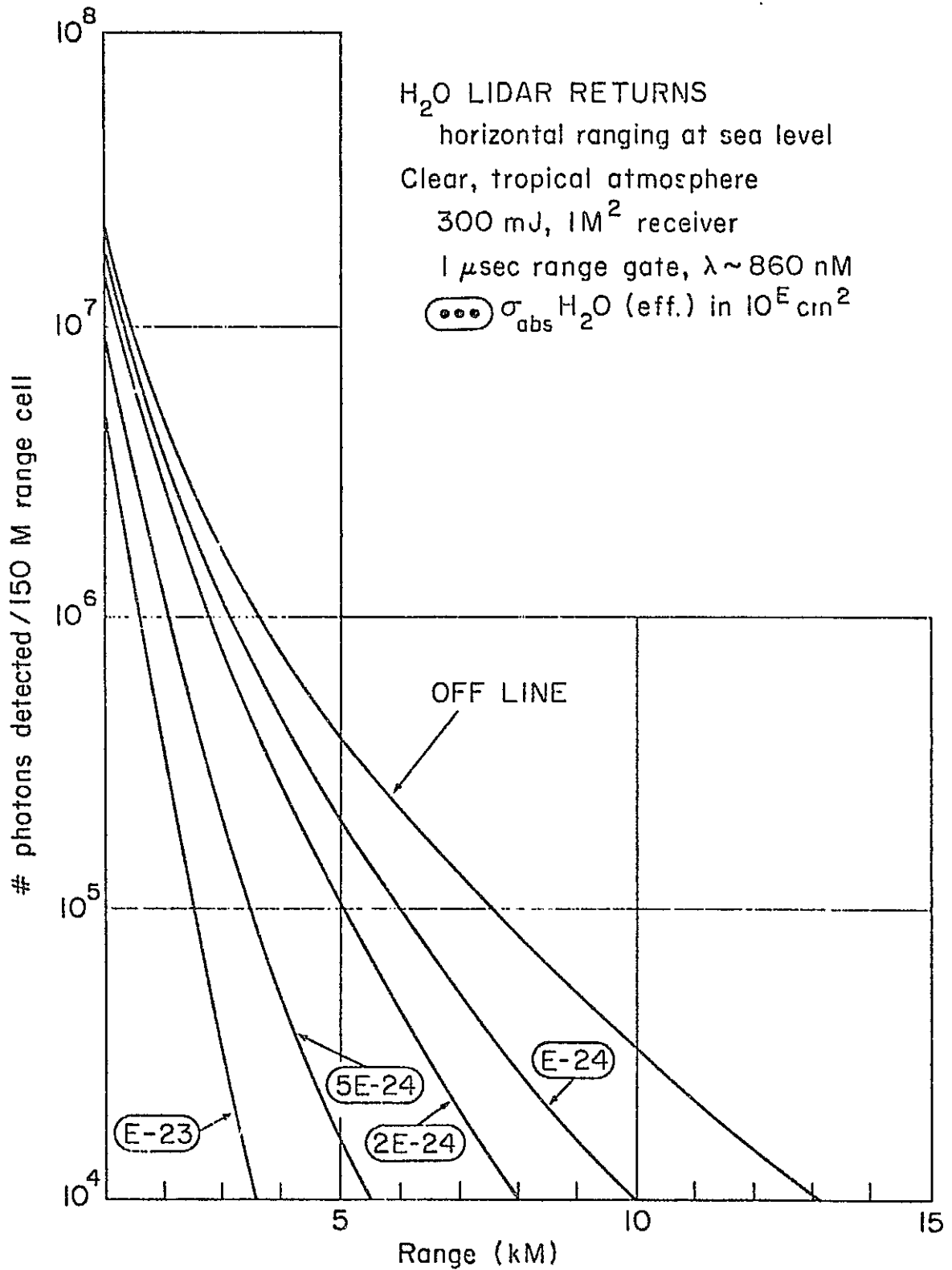


Figure 6

to the logarithmic derivative which must be calculated from such signals in order to extract $[H_2O]$ (see Equation 6).

Figures 7 and 8 deal with the opposite extreme of stratospheric observations by horizontal ranging from aircraft. Figure 7 compares the off line returns to be expected from the molecular atmosphere at 20 km altitude and a Rayleigh-scattering aerosol whose concentration is $30/cm^3$. Variations in an aerosol concentration of this magnitude at this altitude will clearly dominate the molecular backscatter contribution. Assuming only the molecular off line return, Figure 8 shows the large water vapor absorption cross sections required to render 5 ppm of H_2O detectable in the stratosphere. These H_2O cross sections can be obtained further into the infrared, or at high altitude for the 9400 \AA lines owing to line-narrowing at the greatly reduced ambient pressure in the stratosphere.

Figures 9 and 10 estimate the lidar returns to be expected at South Pole Station (ground level $\sim 3\text{kM}$ altitude) in the summer when there is a low altitude, large particle aerosol abundance of order 150 cm^{-3} (W. Zoller, private communication). Mie backscatter is assumed to apply, having a magnitude roughly $1/5$ that for Rayleigh-scattering particles. Thus the aerosol return here is about the same as in the stratospheric case shown in Figures 7 and 8, while the molecular backscatter is much larger owing to the higher atmospheric pressure.

The distinct on line return for H_2O , in spite of the low value of $[H_2O] \sim 2 \times 10^{15} \text{ cm}^{-3}$, is due to the large absorption cross section assumed, which is appropriate for lines in the vicinity of 9400 \AA (see subsection 3.2). We conclude that lines of this strength are mandatory for water vapor assay in the polar regions, and that weaker lines at shorter wavelength are not

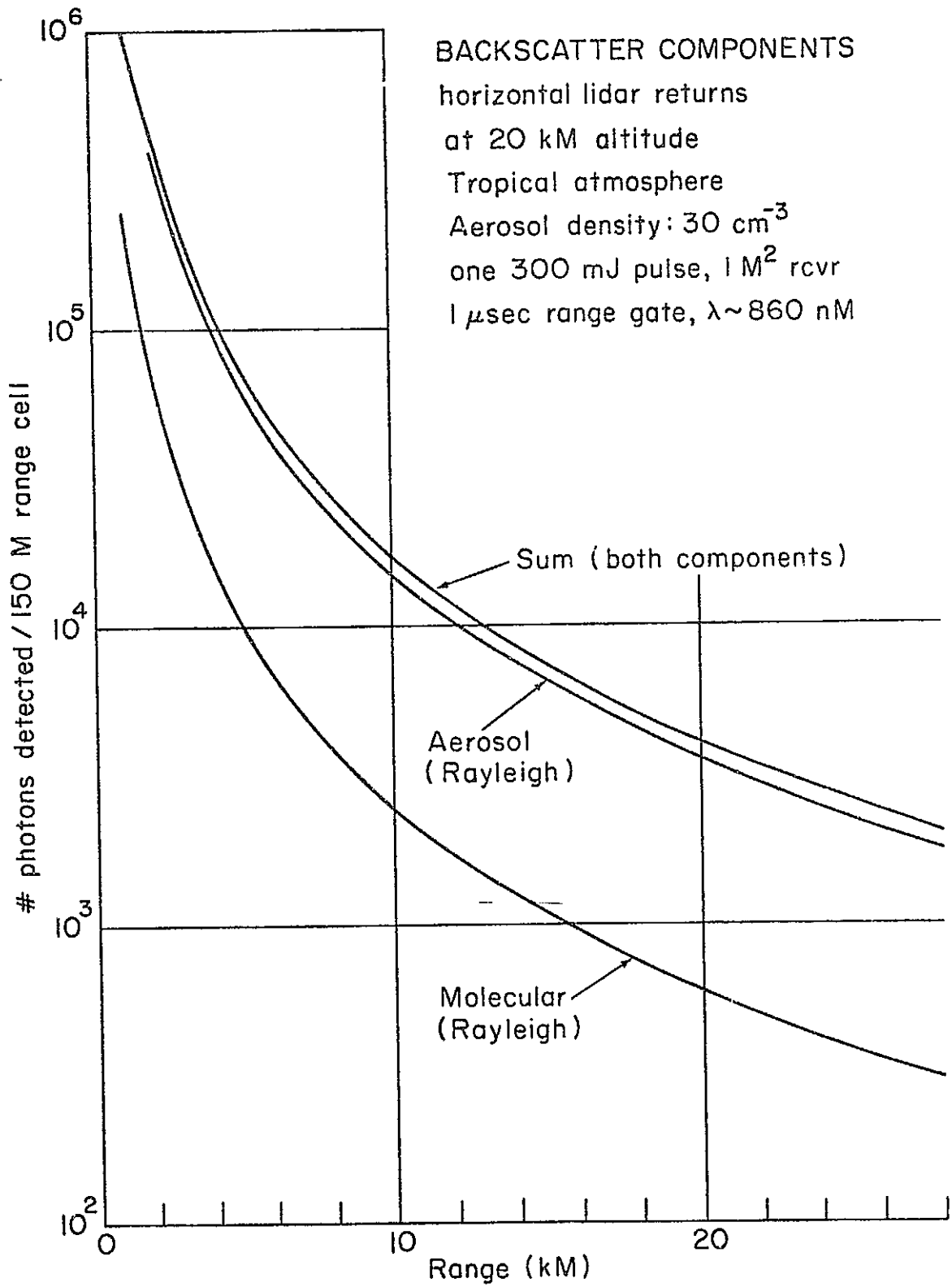
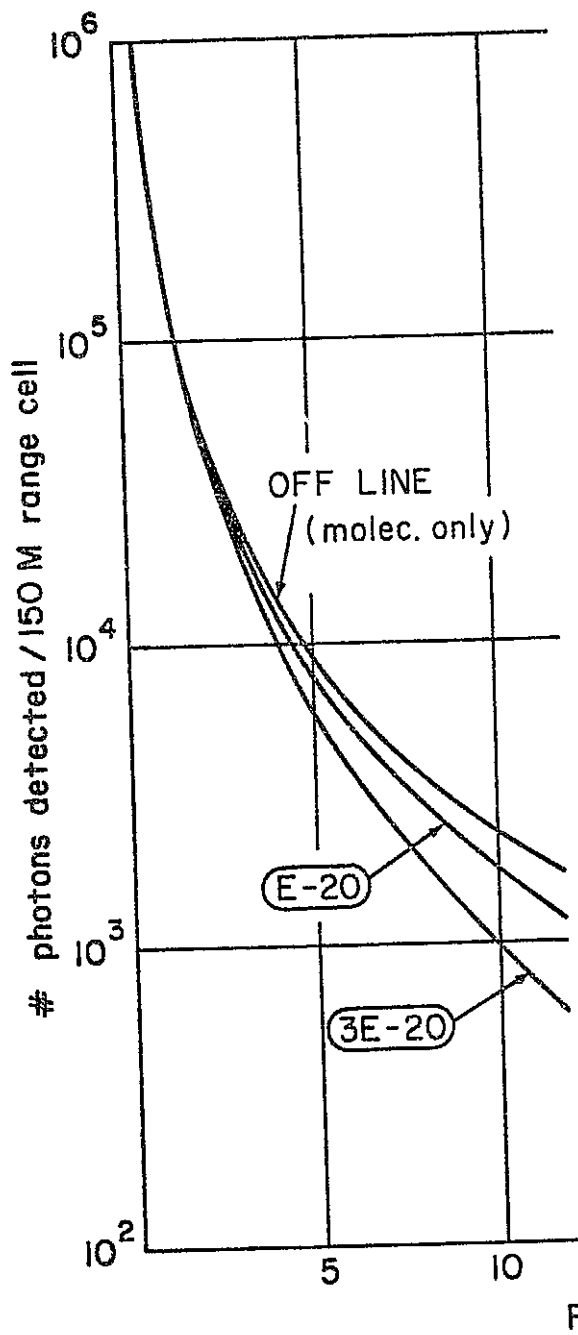


Figure 7



H₂O LIDAR RETURNS
 horizontal ranging at
 20 km altitude
 Tropical atmos., 5 ppm H₂O
 molecular backscatter only
 300 mJ, 1M² rcvr. area
 1 μsec range gate
 λ ~ 860 nm
 (●●●) σ_{abs} H₂O (eff.) in 10^E cm²

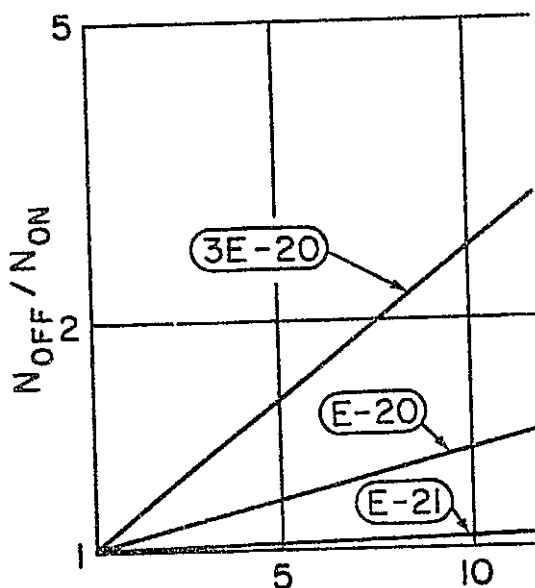
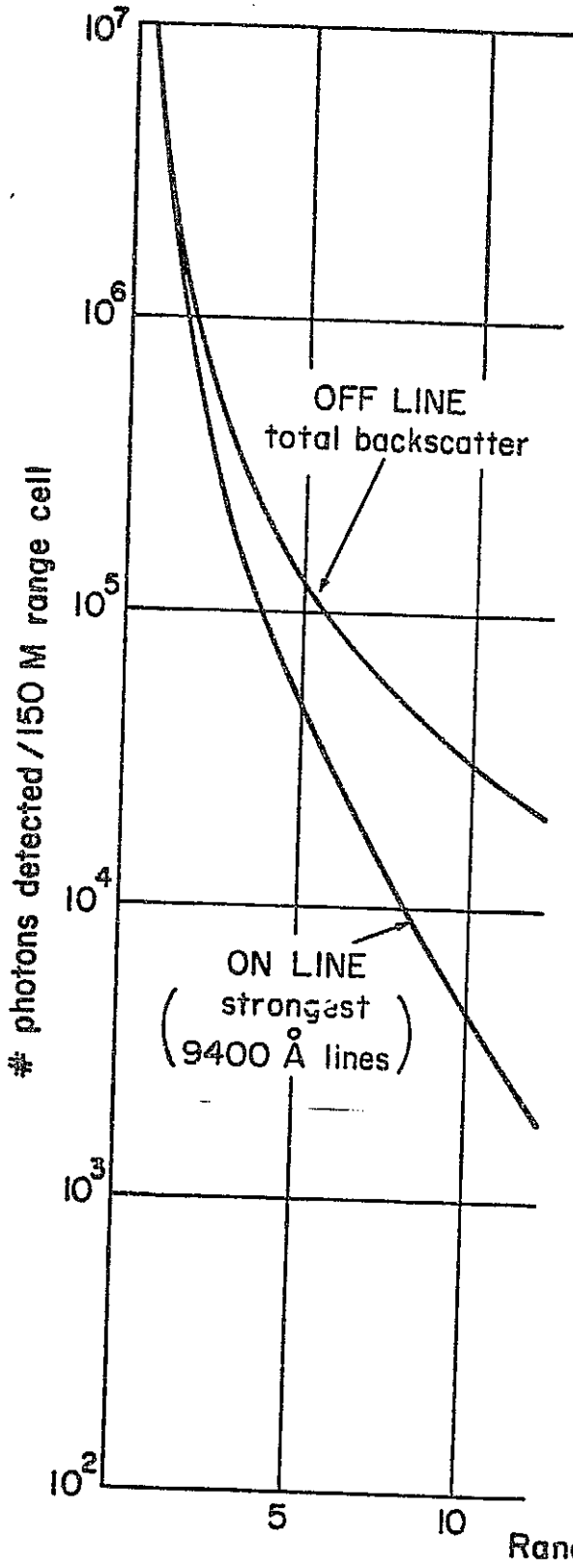


Figure 8



H₂O LIDAR RETURNS
horizontal ranging
at South Pole Station
Antarctic Summer
aerosol density: 150 cm^{-3} (Mie)
H₂O density: $2 \times 10^{15} \text{ cm}^{-3}$
300 mJ, 1 M^2 rcvr. area
 $1 \mu\text{sec}$ range gate, $\lambda \sim 860 \text{ nM}$
 $\sigma_{\text{abs}} \text{ H}_2\text{O} = 5 \times 10^{-22} \text{ cm}^2$

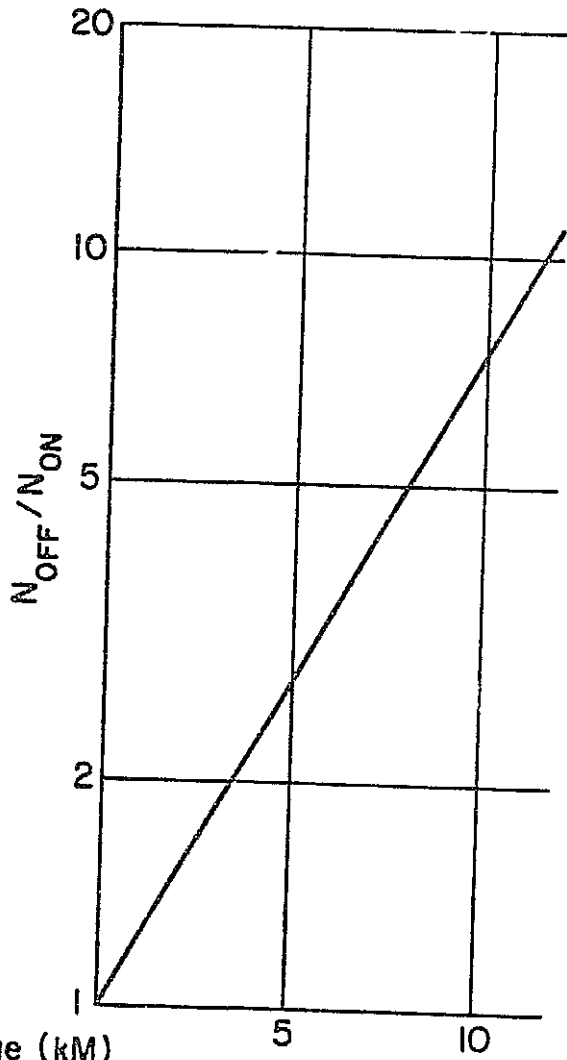


Figure 9

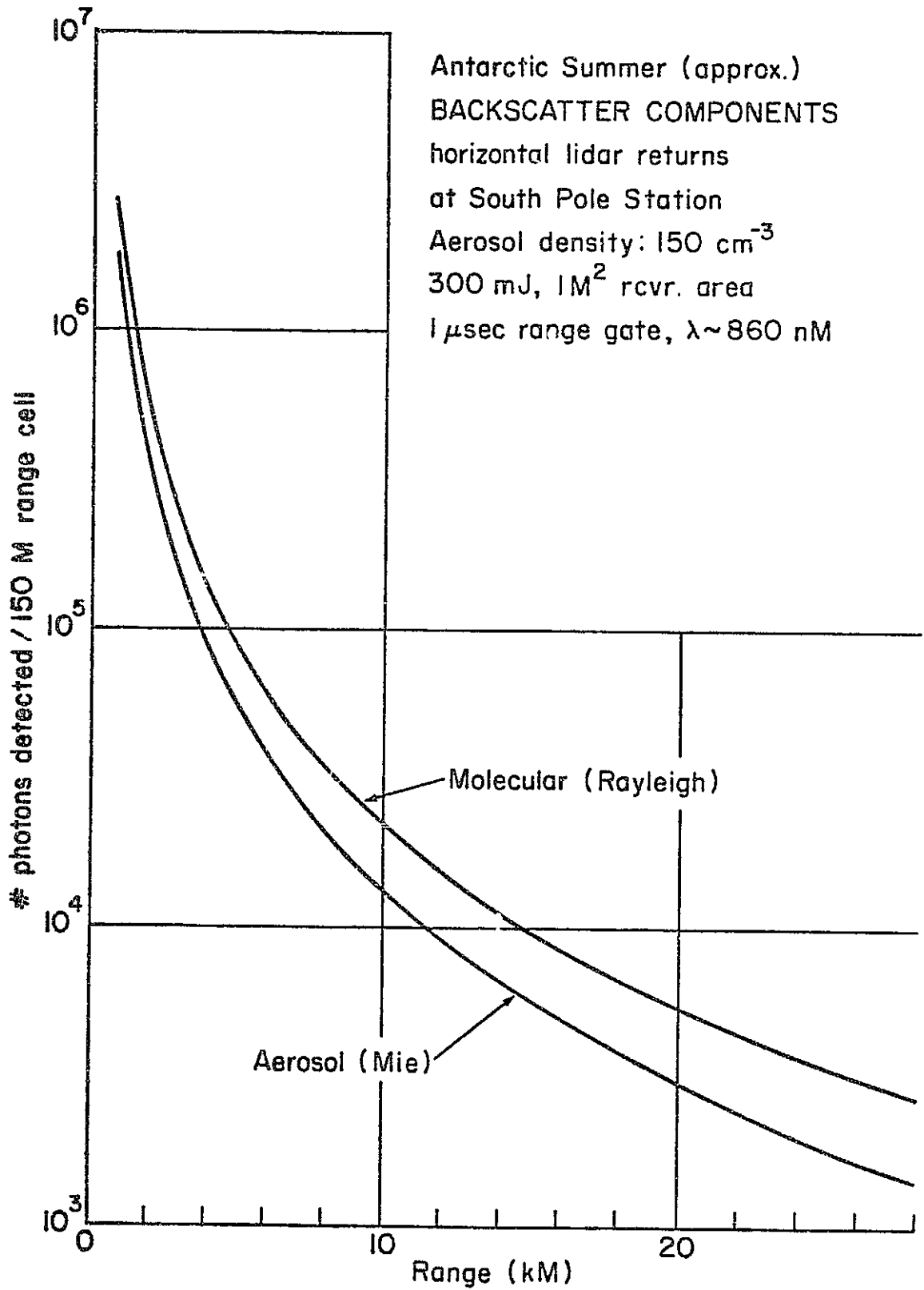


Figure 10

suitable for this type of lidar operation.

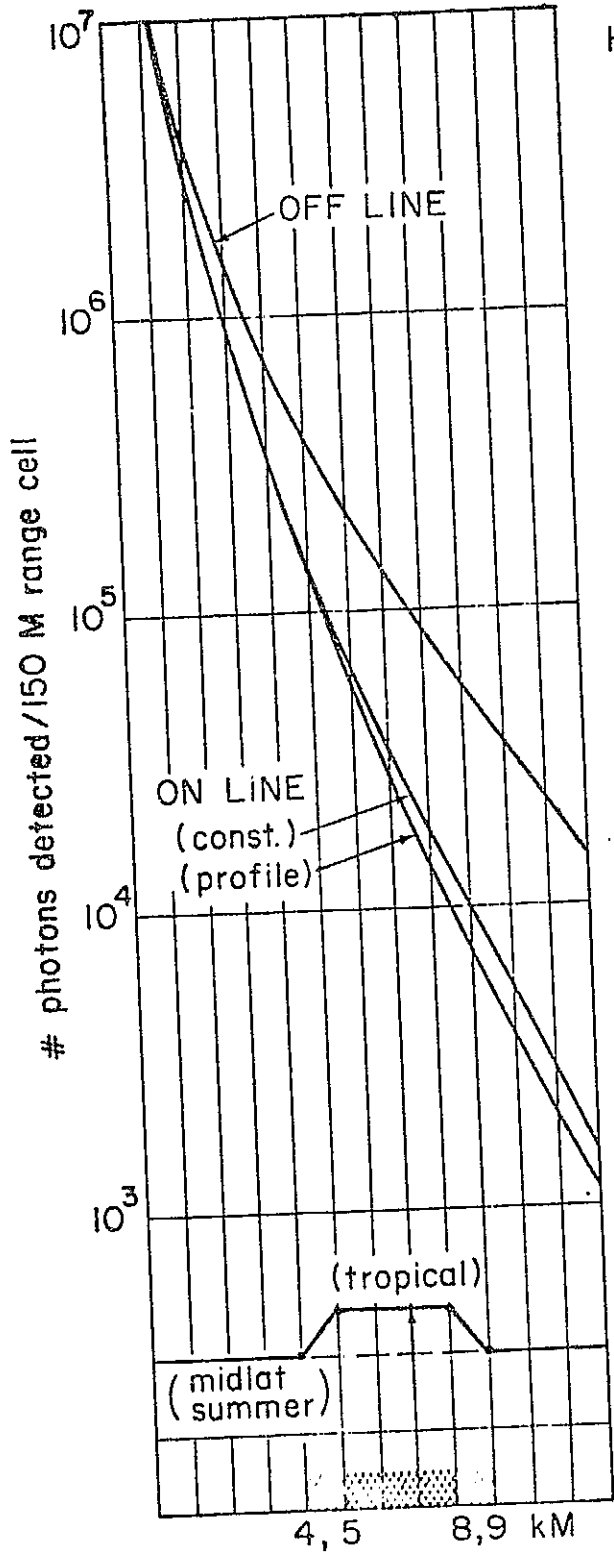
3.3.2 Detection of Humidity Variations (horizontal ranging)

Several lidar calculations are given here having to do with the "visibility" of humidity variations in a uniform or varying aerosol background. Figures 11, 12 and 13 compare three altitude cases in which the aerosol distribution is uniform (clear) along the line of sight while the humidity increases in a well-defined "bump" between 4 and 9 km range. Figures 11 and 12, for sea level and 3 km altitude in a midlatitude summer atmosphere, show the effects of a humidity profile which locally achieves a tropical level appropriate to each respective altitude. Figure 13 at 10 km assumes 20% and 60% humidity increases above the background value.

Aside from the characteristic shift of the off line returns as the extinction coefficient diminishes with altitude, the main difference in the three figures is the value of the H_2O absorption cross section required to give a distinct humidity signature in the presence of the variable profile. The range of cross sections is compatible with near infrared operation.

In the case of Figure 11, the on line signal changes by about 3% by the time one is observing the 5 km range position of the fully developed profile. This change is about 10x the signal shot noise in the corresponding range gate.

It seems likely that lidar operation in the very near infrared will be useful for detecting water vapor profiles connected with developing regions of precipitation or upwelling of moist air. These will be natural objects of study during the development and testing of lidar systems for Space Shuttle application.



H₂O LIDAR RETURNS
horizontal ranging
at sea level
Clear, midlatitude summer
300 mJ, 1 M² rcvr. area
1 μsec range gate
 $\lambda_{\text{off}} = 860 \text{ nm}$
 $\sigma_{\text{abs.}}(\text{H}_2\text{O}) = 2 \times 10^{-24} \text{ cm}^2$

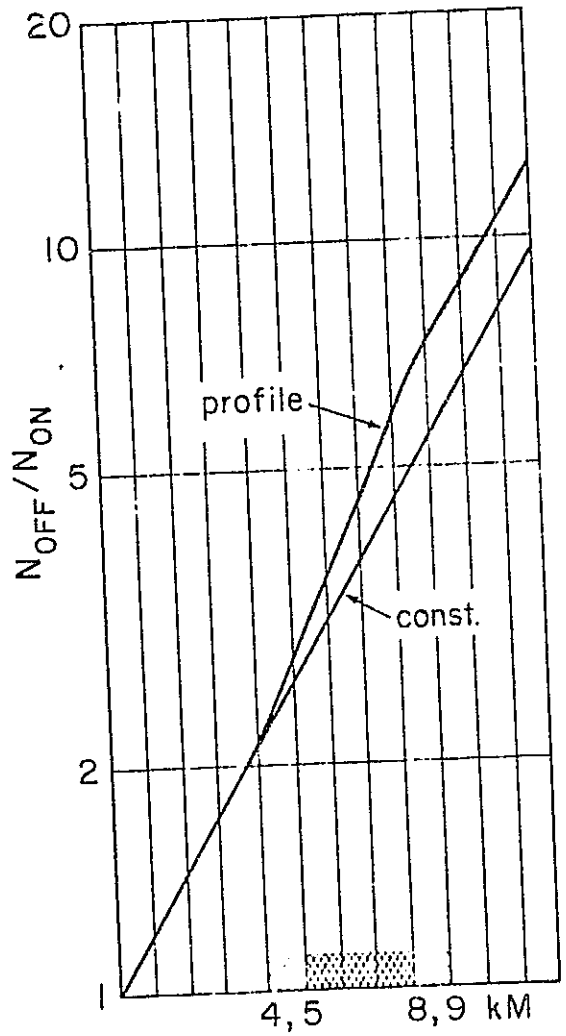
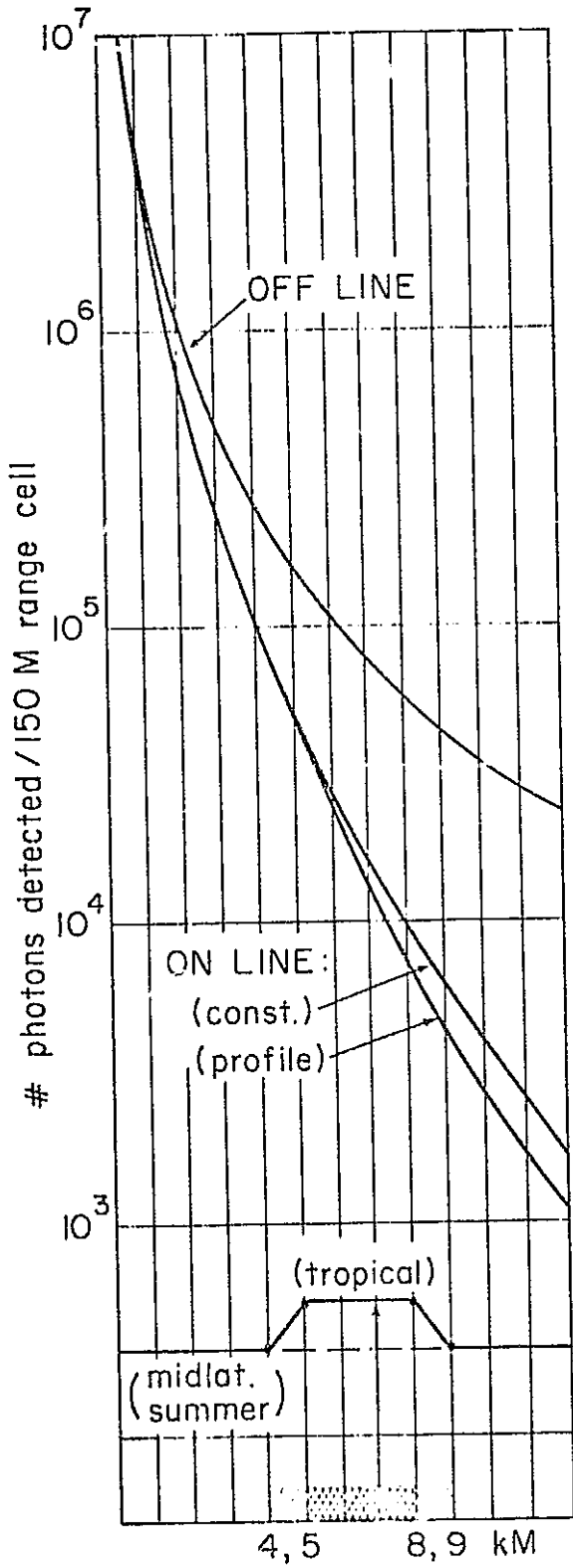


Figure 11



H₂O LIDAR RETURNS
horizontal ranging at
3 km altitude
Clear, midlatitude summer
300 mJ, 1M² rcvr. area
1 μsec range gate
 $\lambda_{\text{off}} = 860 \text{ nm}$
 $\sigma_{\text{abs.}}(\text{H}_2\text{O}) = 10^{-23} \text{ cm}^2$

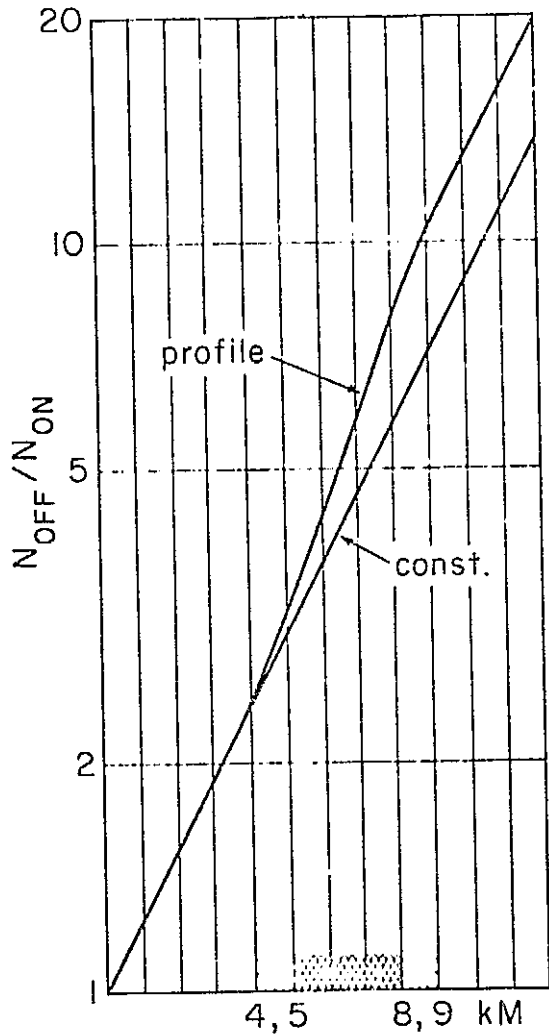
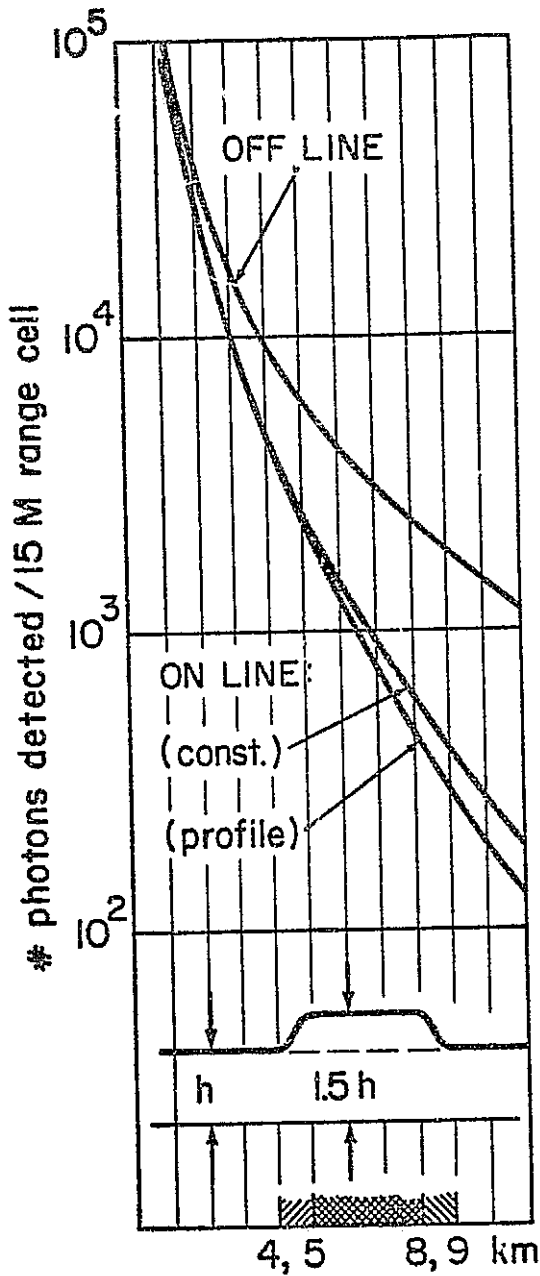


Figure 12



H₂O LIDAR RETURNS
horizontal ranging
at 10 km altitude
Clear, tropical atmos.
300 mJ, A = 1 M²
100 nsec range gate
 $\lambda \sim 700 - 1000 \text{ nM}$
 $\sigma_{\text{abs}} \text{H}_2\text{O} = 5\text{E}-22 \text{ cm}^2$

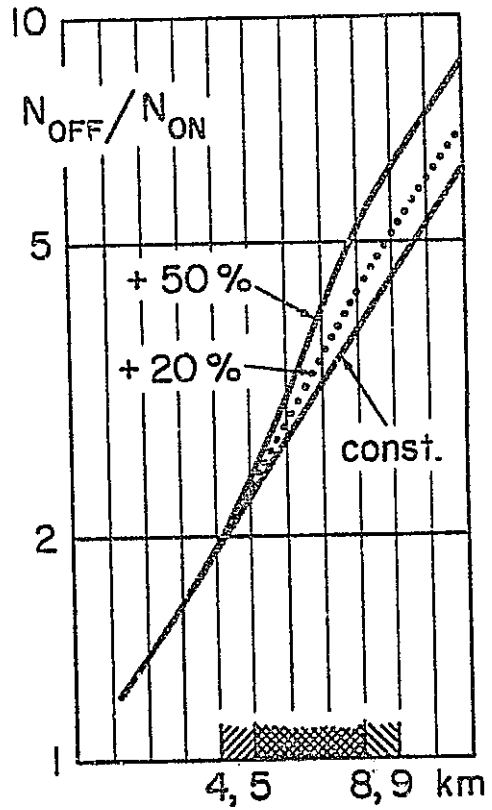


Figure 13

REPRODUCIBILITY OF THE
ORIGINAL PAGE IS POOR

Figures 14 - 17 depict the different types of lidar returns one will encounter when both the aerosol and water vapor concentrations vary along the line of sight. Various combinations of (clear, hazy) and (tropical, midlatitude summer) are considered. Figures 14 and 15 show the probing of the edge of a large region of atmospheric variation, such as one might encounter in horizontal ranging perpendicular to a sea coast. The manifest non-parallelism of the on line and off line returns implies measurability of $[H_2O]$ in these gradient regions, given sufficient transmitted laser energy. Figures 16 and 17 are concerned with mutual and opposite variations of aerosols and water vapor, over "bump" portions of the atmosphere which are roughly as large as they are distant from the lidar station. The lidar signatures are very different, and again admit of water vapor measurements if one employs sufficient laser energy. While the accuracy of these particular measurements is not assessed here, it is clear from the variability of these signatures between different atmospheric models that many types of situations can be distinguished from one another in field operations.

3.3.3 Vertical Ranging from Ground Stations

For both this case and the Shuttle case (3.3.4) it was necessary to represent the altitude variation of the pertinent optical properties of the earth's atmosphere; viz. the extinction and backscatter due to aerosols and molecules, and the line absorption due to water vapor. Our emphasis has been to establish feasibility rather than to obtain extremely accurate simulations of lidar returns. Therefore we have assumed H_2O absorption cross sections which do not depend on altitude, as well as employing the model wavelength of $8600\overset{\circ}{\text{A}}$ and the "1/5 X isotropic" assumption for backscatter by Mie-scattering aerosols. The present calculations therefore

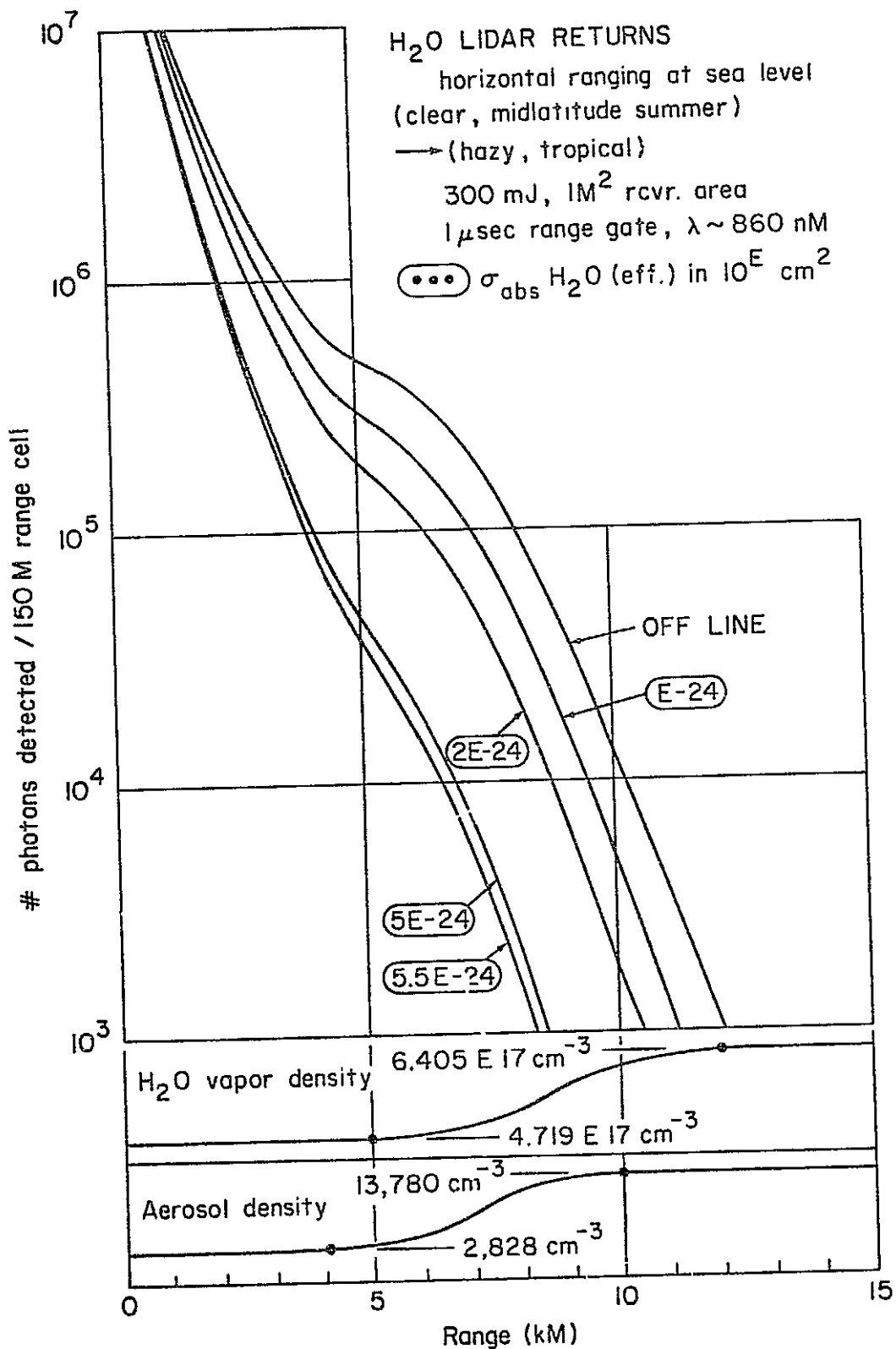


Figure 14

REPRODUCIBILITY OF THE ORIGINAL PAGE IS POOR

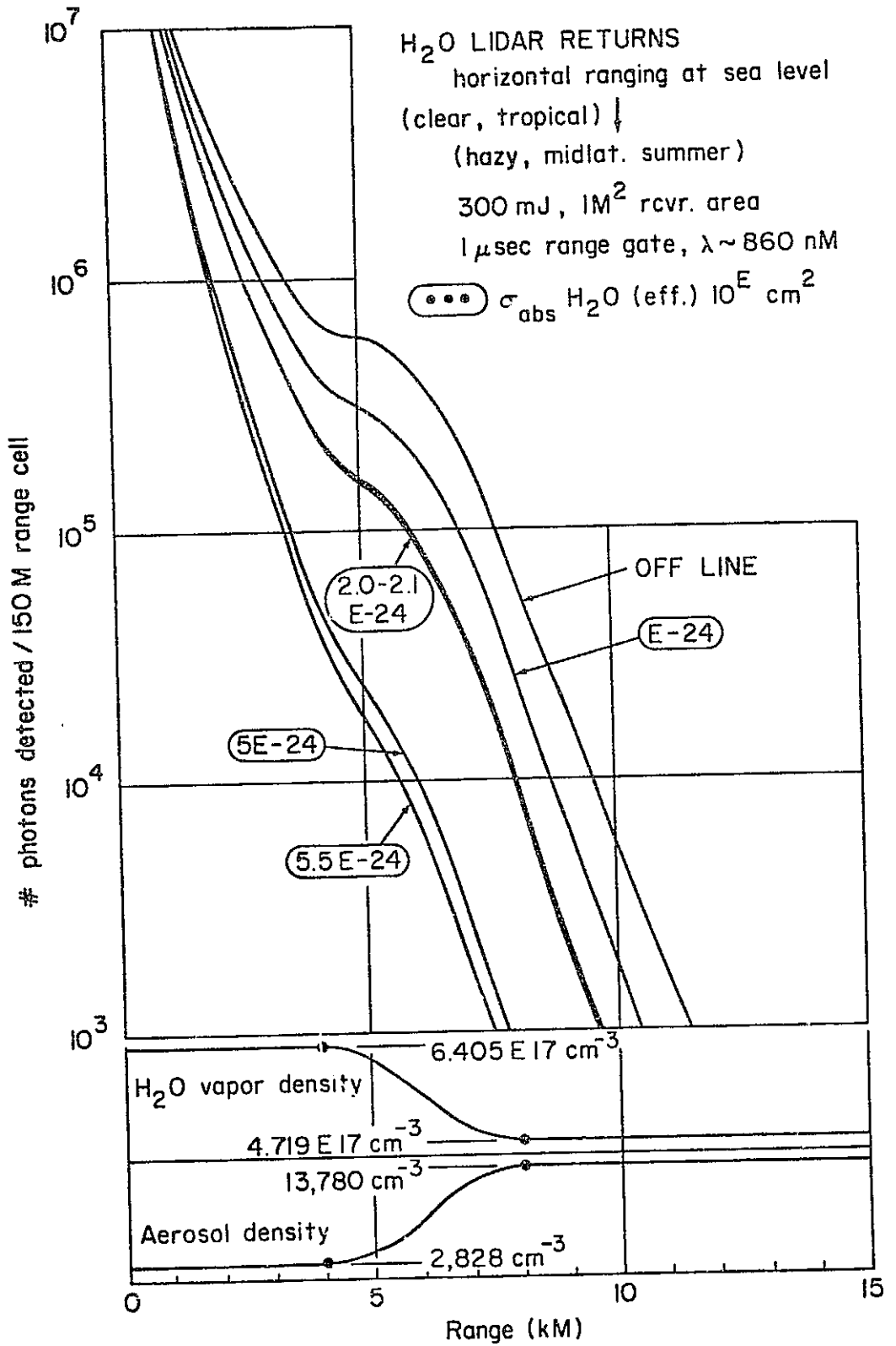


Figure 15

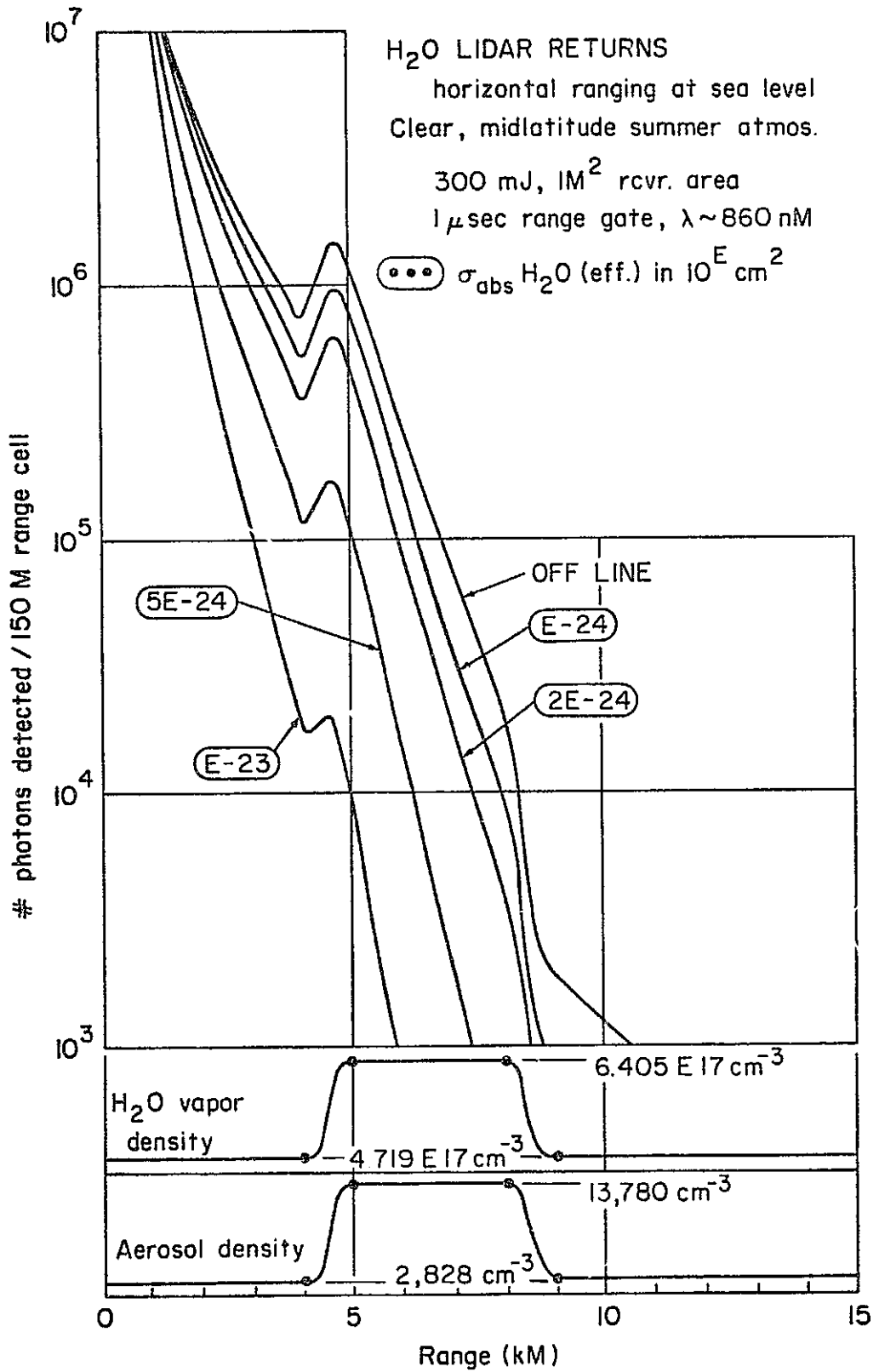


Figure 16

...ITY OF THE
... IS POOR

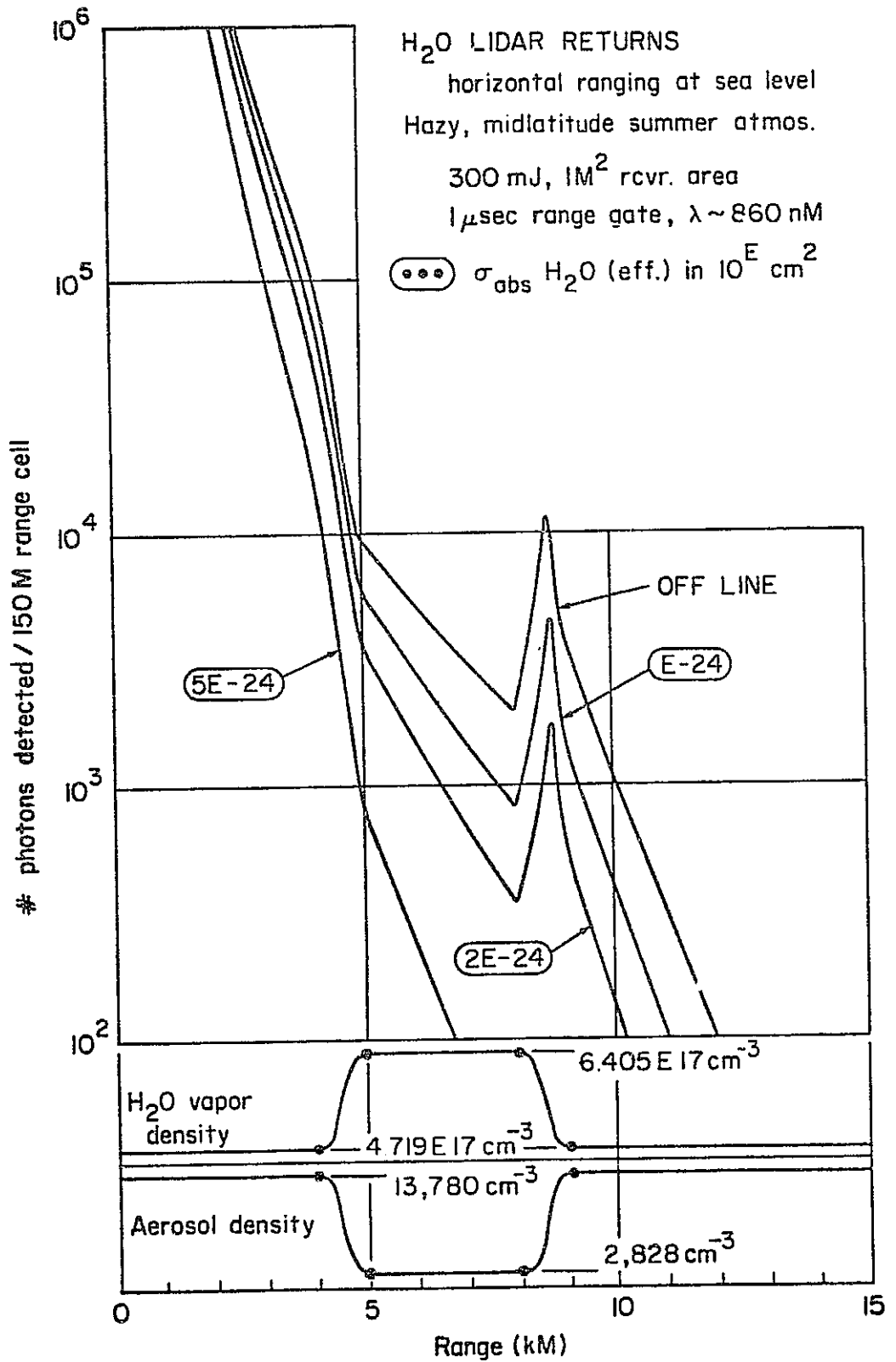


Figure 17

err on the pessimistic side as regards the detectability of H_2O at high altitude, where the lowered pressure and temperature in fact enhance the absorption cross section at line centers λ_{oi} and therefore impart a larger optical depth β_{oi} to laser radiation tuned to λ_{oi} .

Table 5 shows the curve - fitting relations which were employed in order to carry out the full lidar simulations on a Hewlett-Packard 9810/9862 calculator/plotter. Information on these programs will be reported in the near future and will in the meantime be available on special request.

Figure 18 shows the total off line return for a ground based lidar operating near $\lambda = 8600 \text{ \AA}$, ranging upward into a standard clear, midlatitude summer atmosphere. Also, fictitious returns are shown for purely aerosol or purely molecular scattering and extinction. Figure 19 then shows the corresponding on- H_2O -line returns for different absorption cross sections, compared to the off line return. Figure 20 shows the ratios (off line/ on line) as functions of range and cross section.

The marked rate of decrease in signal at low altitude is due to the preponderance of aerosols there, as contrasted to the slower fall off at higher altitude where molecular backscatter is dominant. It is clear that upward-ranging lidar experiments will in general present a problem in the dynamic range of measurement. Careful optimization of line strength is required in order to obtain reasonable accuracy in $[H_2O]$ above 2 km; sensitivity to the lower humidity there requires operating the lidar on lines which show a strong extinction relative to the off line return - and which therefore create difficulties in measuring said humidity accurately.

Table 5. Typical Atmospheric Models
(R = altitude in km)

A. Air Molecular Density Profile

<u>altitude (km)</u>	<u>density (gm/cm³)</u>
0-9	$1,220 \times 10^{-0.0459R}$
9-25	$1,900 \times 10^{-0.0662R}$
25-30	$13,684 \times 10^{-0.1005R}$
R>30	$682.63 \times 10^{-0.05764R}$

B. Aerosol Density Profile (Clear: 23 km visibility)

<u>altitude (km)</u>	<u>density (cm⁻³)</u>
0-2	$+65.243R^3 - 26.847R^2 - 1352.7R + 2828 \text{ cm}^{-3}$
2-4	$-65.243(R-2)^3 + 364.61(R-2)^2 - 677.2(R-2) + 537.1$
4-6	$6.8624(R-4)^3 - 26.847(R-4)^2 - 1.6715(R-4) + 119.2$
6-18	$76.804 \times 10^{-0.013917R}$
R>18	$5256.2 \times 10^{-0.11019R}$

C. Water Vapor Profile (Midlatitude Summer)

<u>altitude (km)</u>	<u>density (cm⁻³)</u>
0-10	$6.2E17 \times 10^{-0.24691R} \text{ cm}^{-3}$
10-15	$1.3002E18 \times 10^{-0.38462R}$
15-20	$1.16E14 \times 10^{-0.04525R}$
20-25	$3.0983E12 \times 10^{+0.03445R}$
25-30	$7.3E13 \times 10^{-0.0203R}$
R>30	$1.2053E16 \times 10^{-0.09412R}$

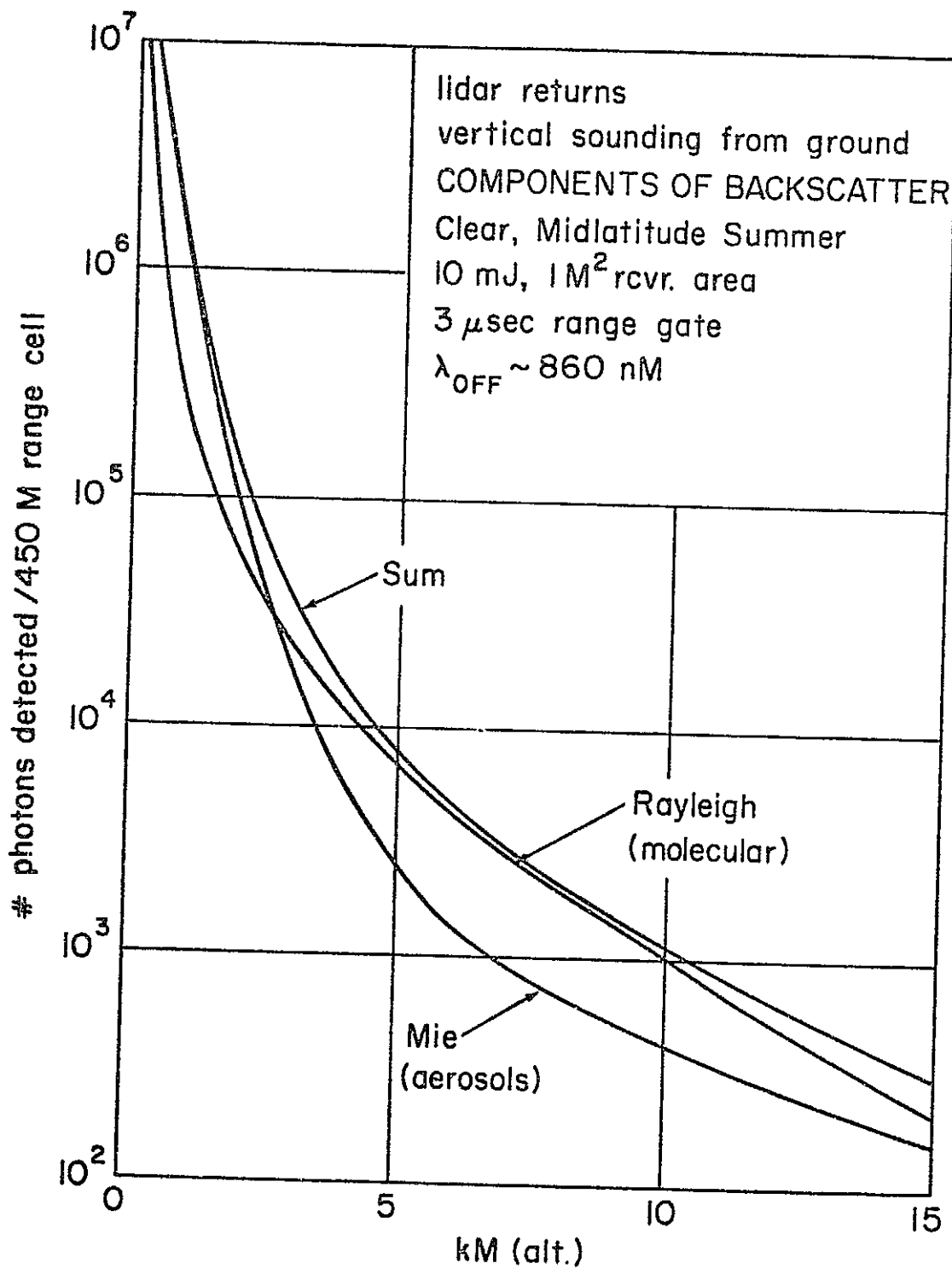


Figure 18

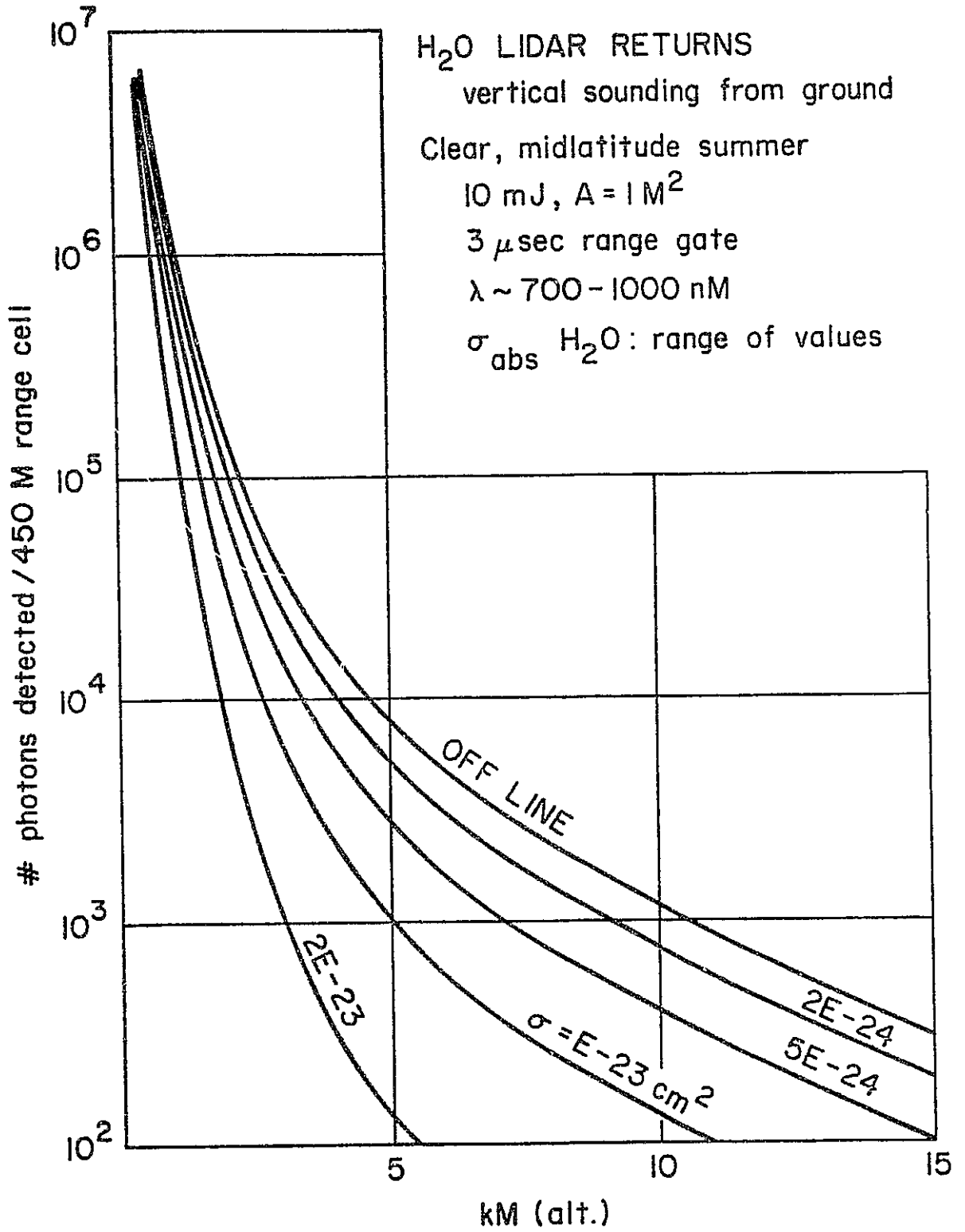


Figure 19

Signal ratio $N_{\text{OFF}}/N_{\text{ON}}(\text{H}_2\text{O})$, $\lambda \sim 700\text{-}1000\text{ nM}$

Vertical sounding from ground, Clear midlatitude summer

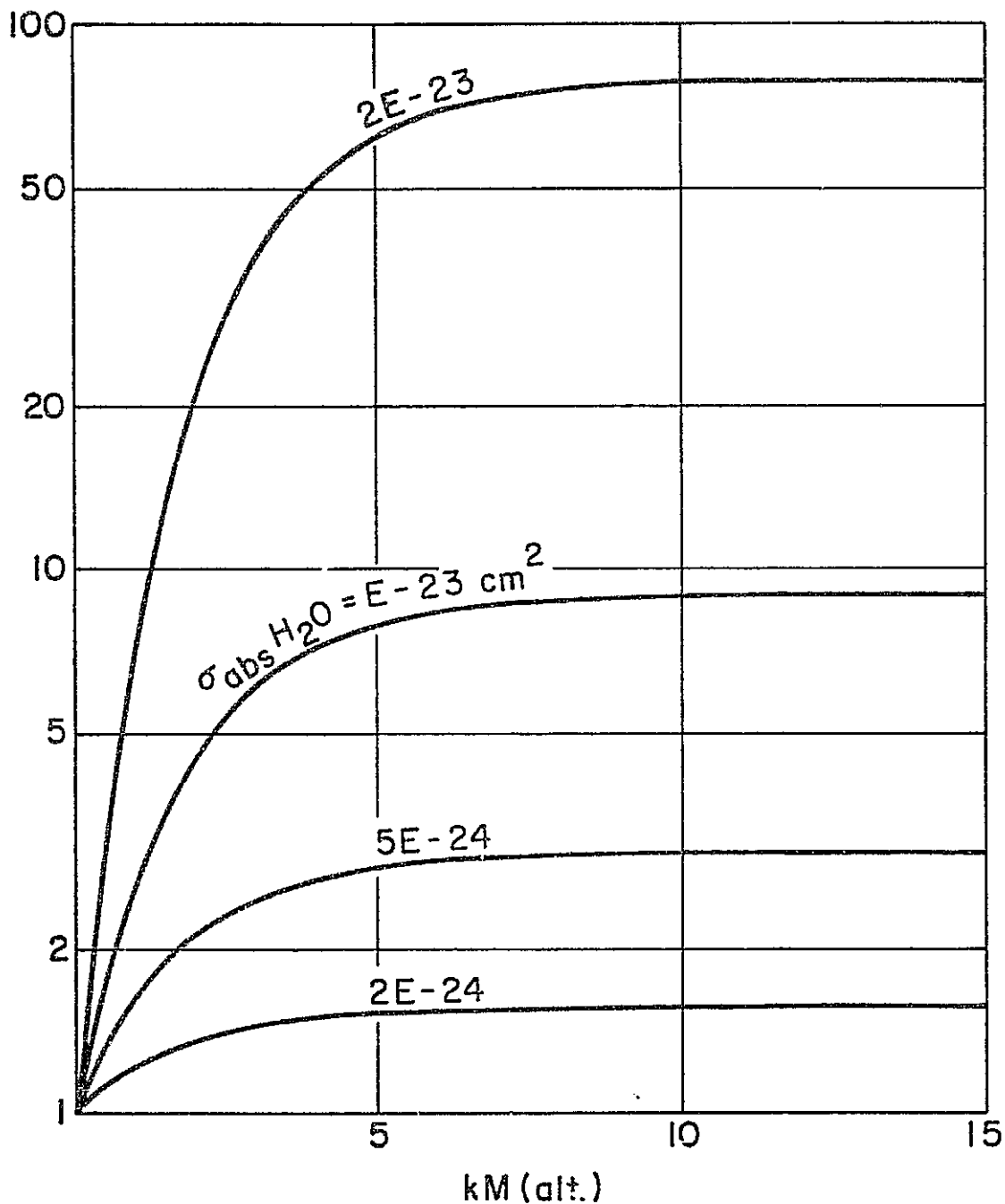


Figure 20

3.3.4 Space Shuttle (downward ranging, 200 km altitude)

By means of the same representations of the atmosphere mentioned in 3.3.3, we have obtained a number of simulations for a water vapor lidar mounted in the Space Shuttle at a (nominal) altitude of 200 km. Figure 21 illustrates the basic, off line returns from the lower atmosphere assuming the two standard haze models used heretofore. The hazy case shown appears to be just about optimum for the maximum lidar return from the bottom of the atmosphere. Figure 22 depicts the good sensitivity to $[H_2O]$, using appropriate cross sections for the several groups of H_2O lines in the near infrared. For these shuttle cases, it is clear that the problem of photon statistics is very pressing and calls for adopting as large a laser energy and lidar receiver as possible so as not to sacrifice range resolution or accuracy of the humidity measurement.

Figures 23 and 24 present a broader picture of the Space Shuttle lidar, for both the hazy and clear midlatitude summer atmospheres. The off line return is followed out to an altitude of 30 km, where only 5 - 6 photons will be detected on the average for the nearly 1/2 km range cell. Above 10 km one needs very large cross sections even to detect, let alone measure, the water vapor. Therefore we conclude that a nadir-looking lidar measurement of $[H_2O]$ will succeed mainly in the troposphere - and conceivable very well there - and probably not in the stratosphere. The use of many lidar pulses is limited by the average laser power permitted in the Shuttle application, and by the desired spatial resolution in the atmosphere. The distance scale of interest in the stratosphere is much larger than at low altitude, so it may be feasible to accumulate several lidar returns to improve the photon statistics for observations at 10 km and above.

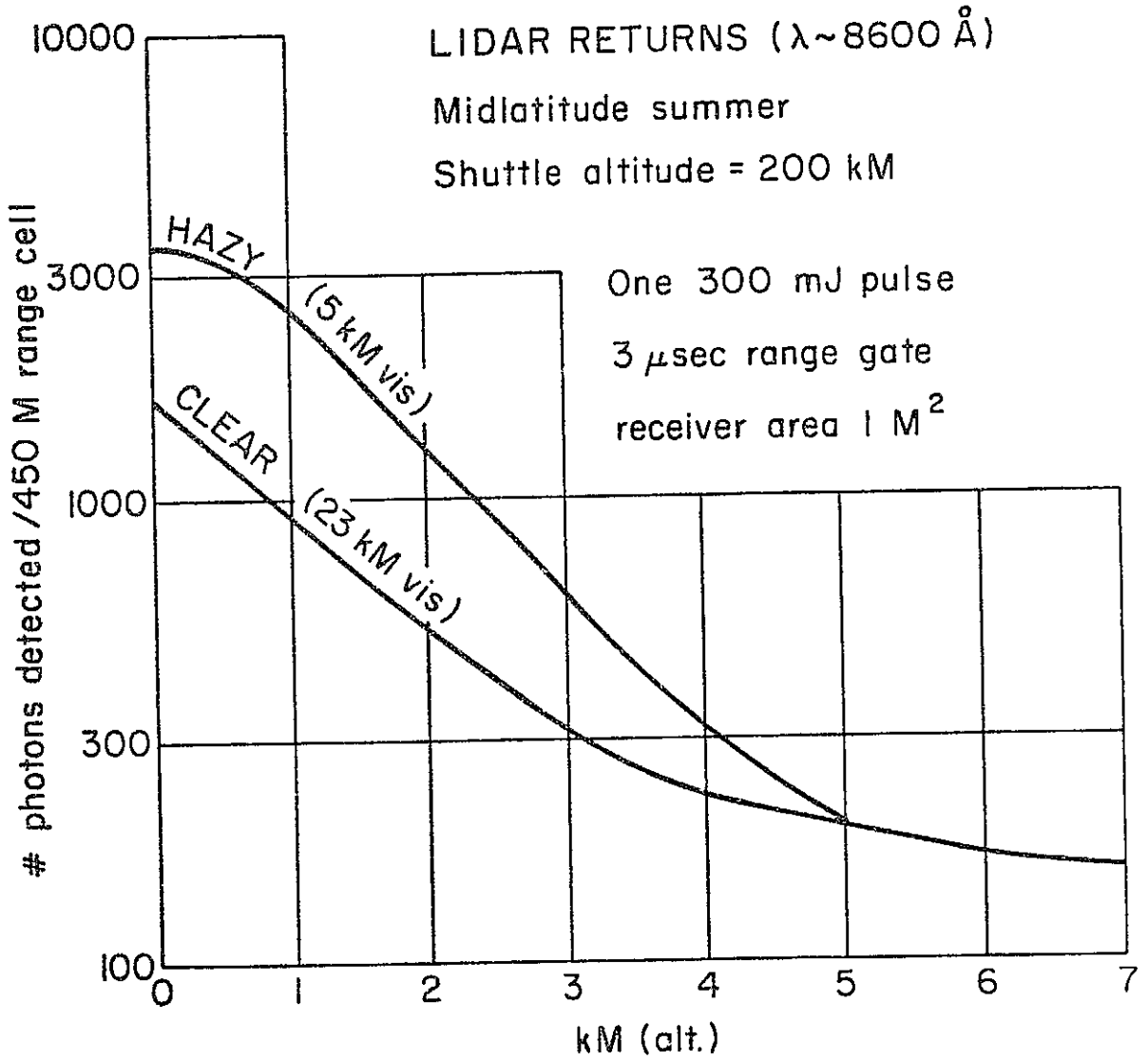


Figure 21

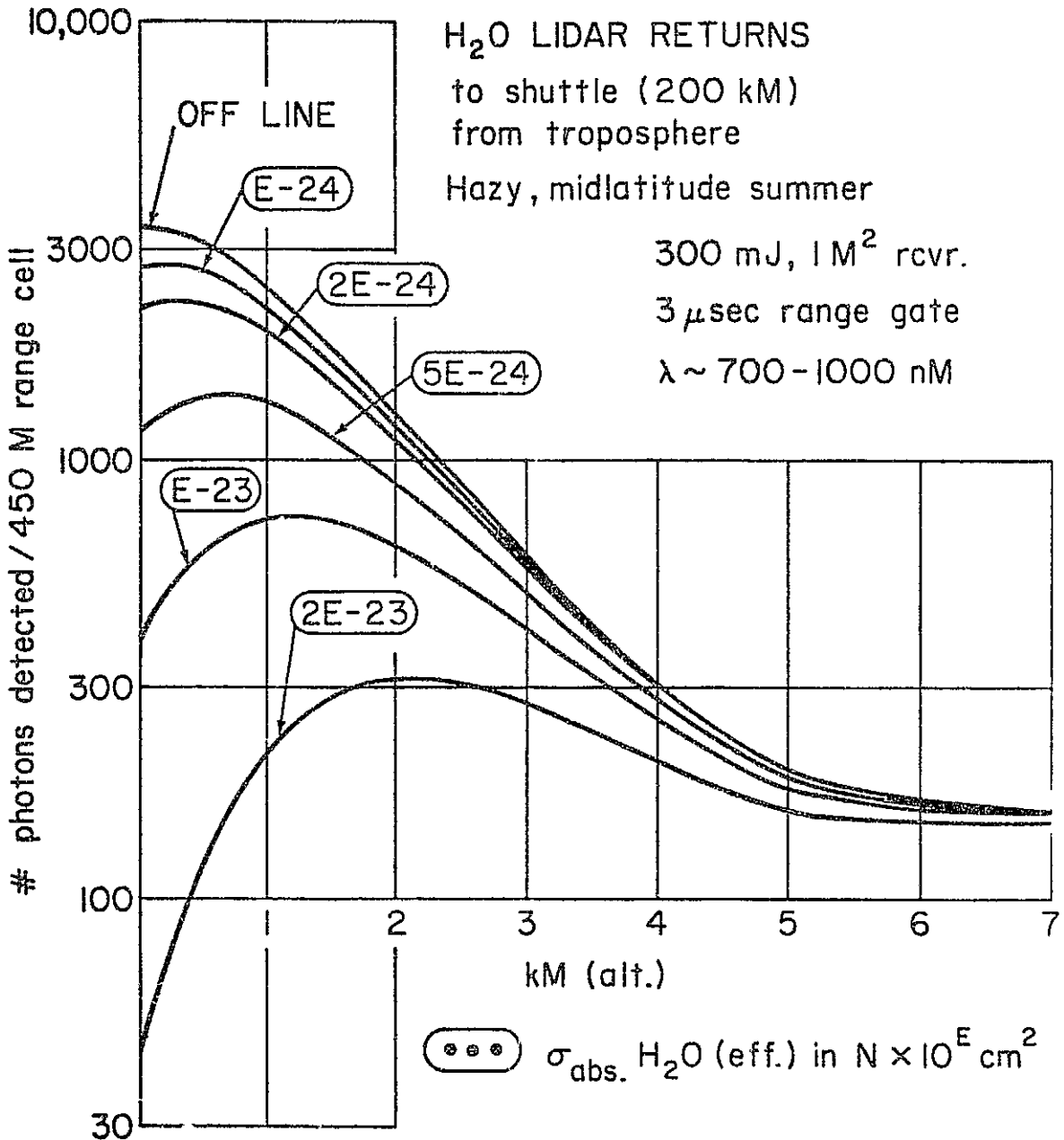


Figure 22

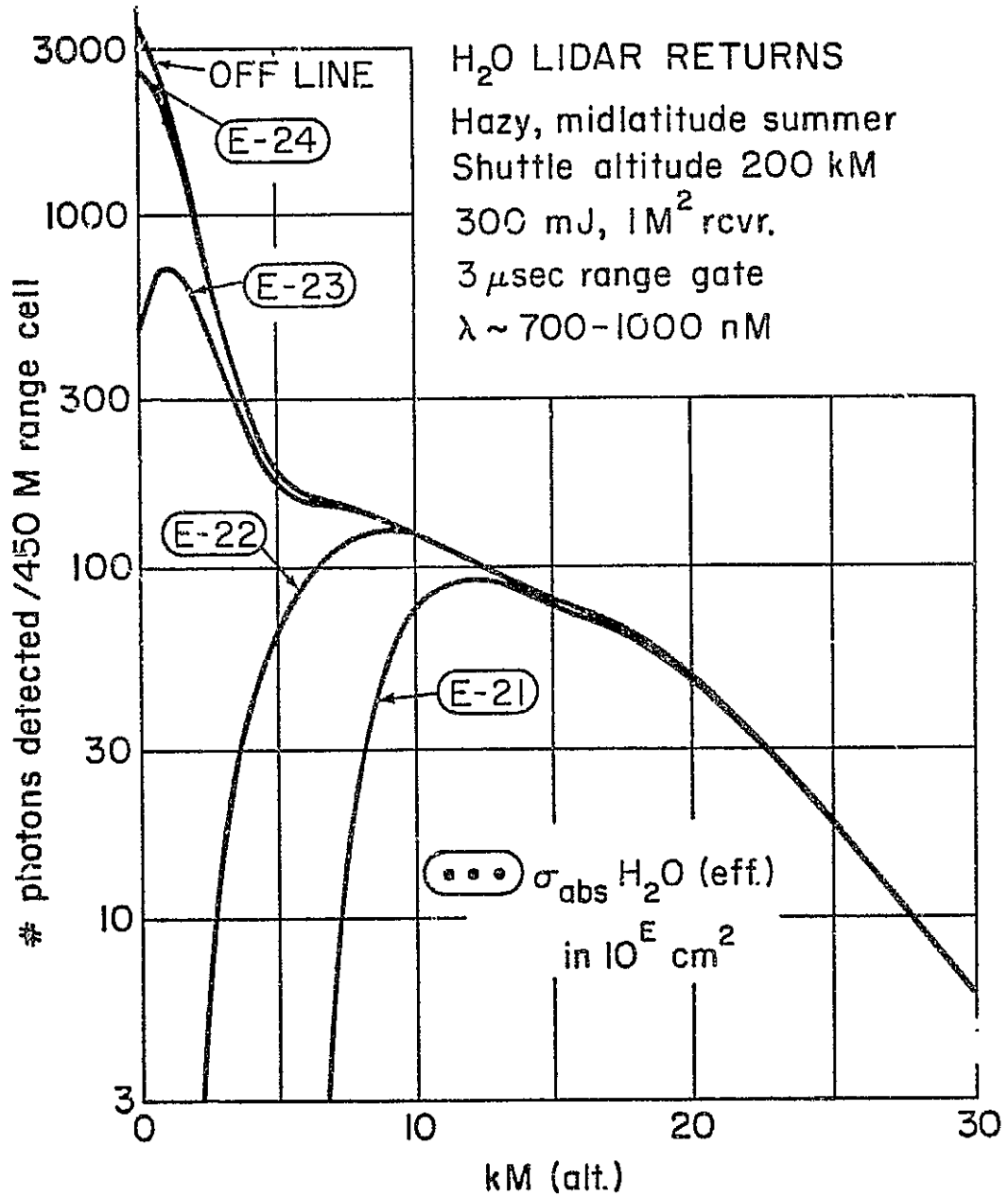


Figure 23

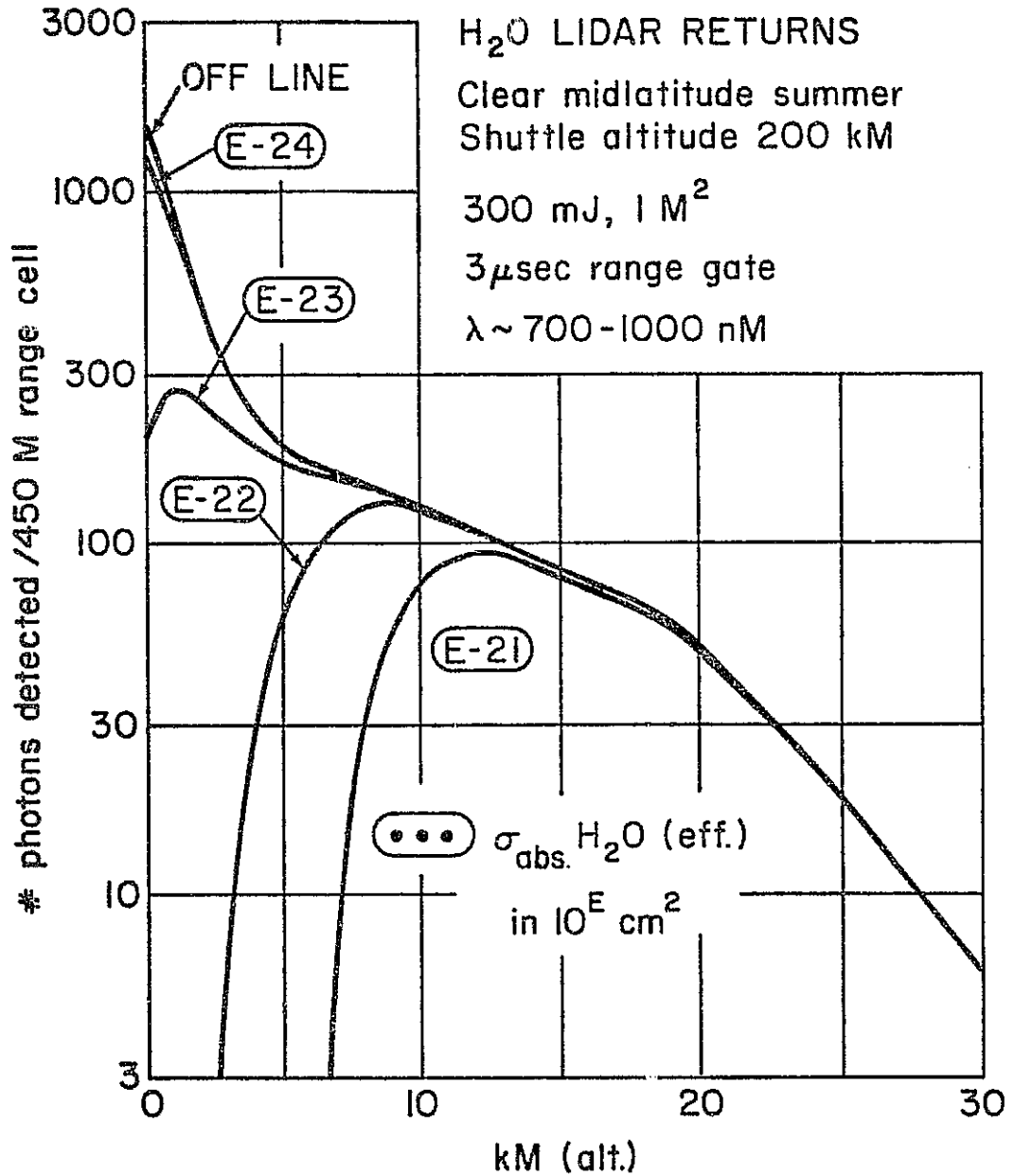


Figure 24

Figures 25 and 26 for a standard tropical atmosphere complement Figures 23 and 24. They demonstrate primarily a slight enhancement of the absorption by H_2O , which would not materially alter the design of such a lidar experiment.

Figure 27 describes the origins of the off line return as seen from the Space Shuttle, in terms of Rayleigh scattering from the molecular atmosphere and (assumed) Mie scattering from aerosols. If in fact the stratospheric aerosols scatter more isotropically than those at low altitude, a stratospheric signal enhancement over the present numbers will result. This, together with increased absorption cross sections owing to line-narrowing in the stratosphere, may make the high altitude assay for $[H_2O]$ more tractable than it seems at present. For this reason, the stratospheric lidar calculation needs now to be tackled via more elaborate representations of the scattering and absorption parameters as functions of altitude.

Figure 28 represents an approximate treatment of orbital lidar soundings over the South Pole, using a simplified atmospheric model to see what a Shuttle-based instrument is capable of in cold regions where the water vapor density is low. Three off line returns are shown for Shuttle altitudes of 100, 150 and 200 km; the backscatter is due to molecules and two aerosol layers whose extents are indicated on the figure. The upward jump near ground level (3 km) is not a ground return from snow and ice, but arises from low level aerosols below a 600 M inversion layer. Three on line returns are shown with the 200 km curve; the highest of these is appropriate for the 9400 Å lines alluded to earlier.

From these curves it is clear that water vapor assay can be carried out from orbit in the polar regions, and that reasonably strong H_2O lines

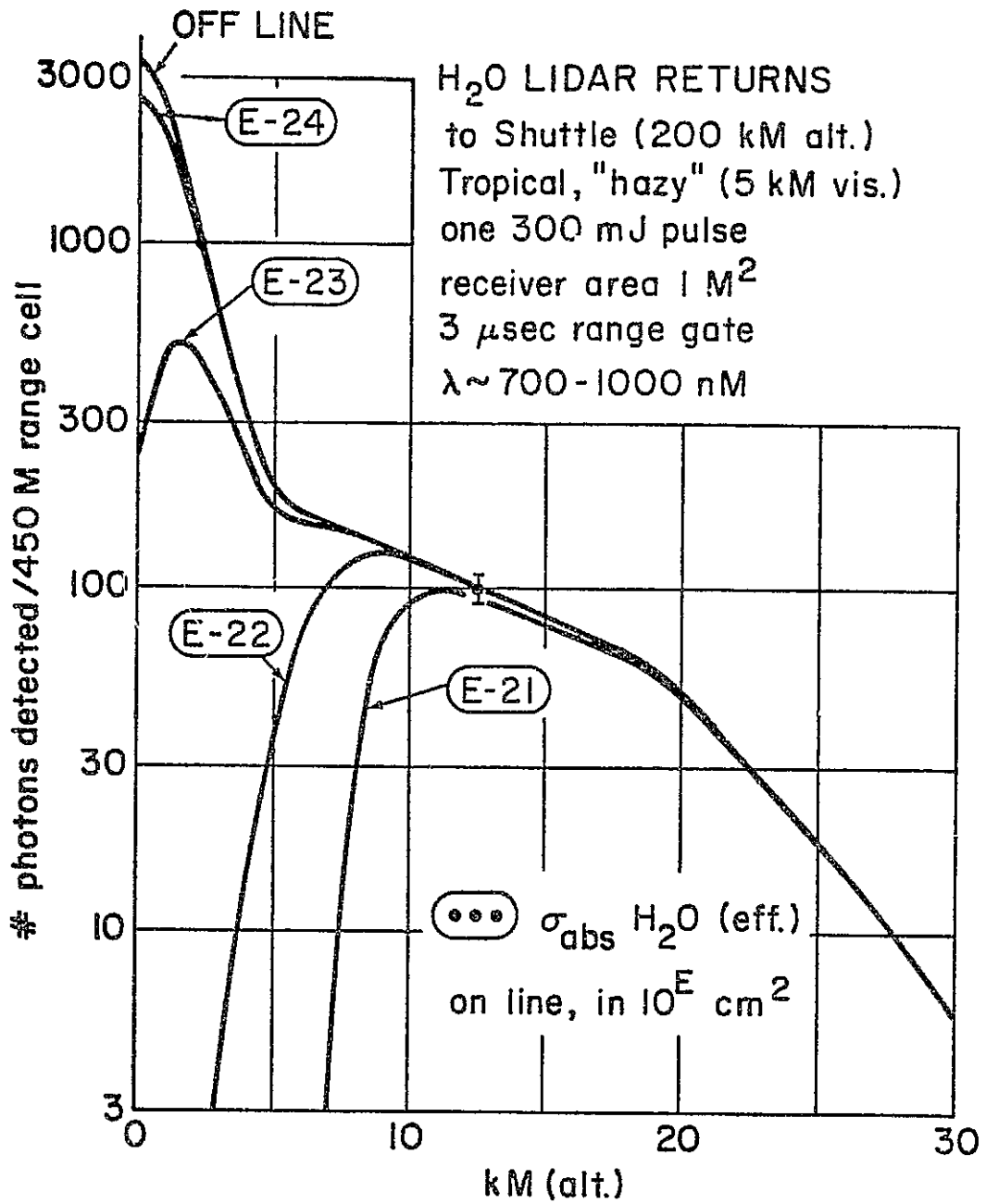


Figure 25

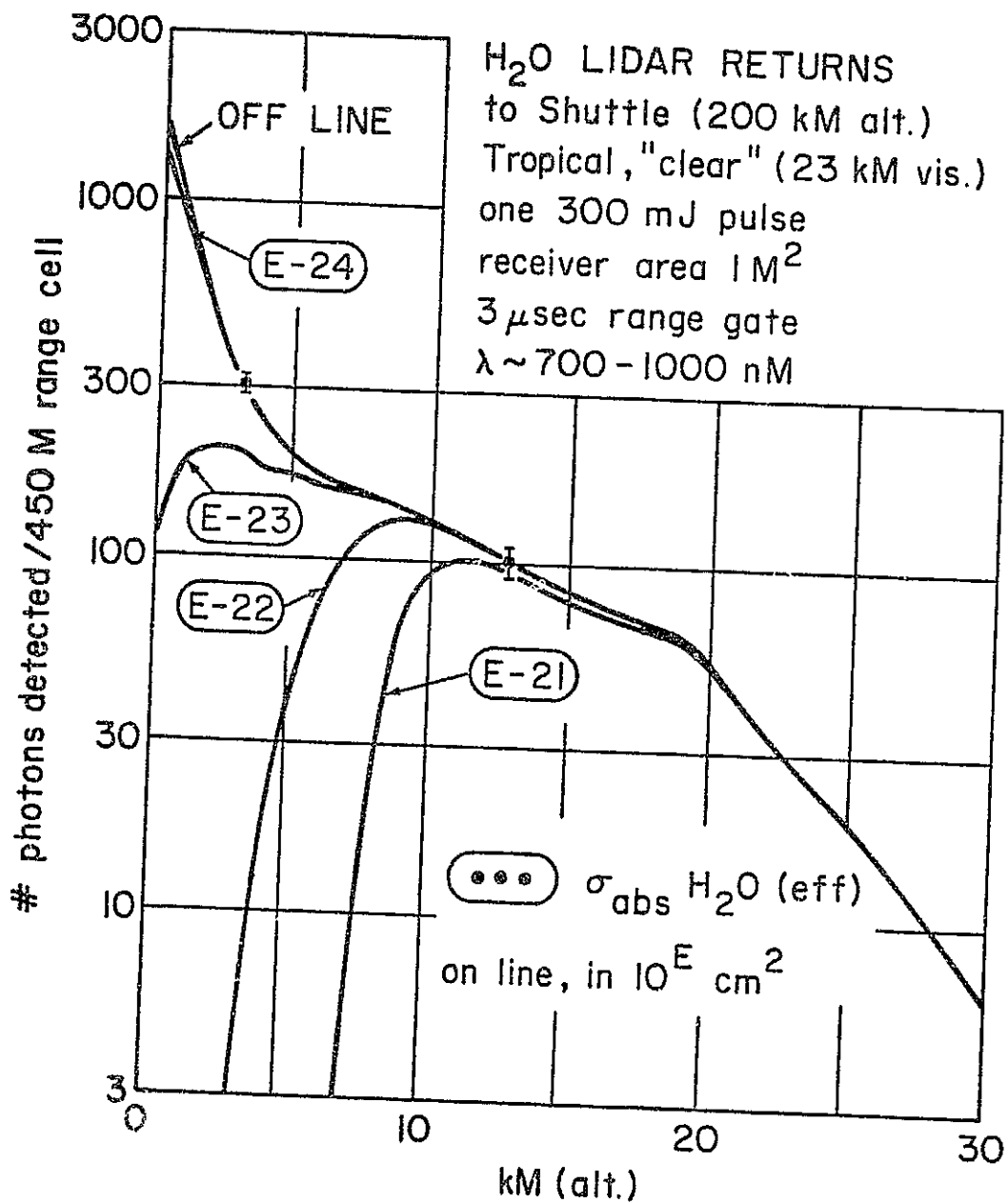


Figure 26

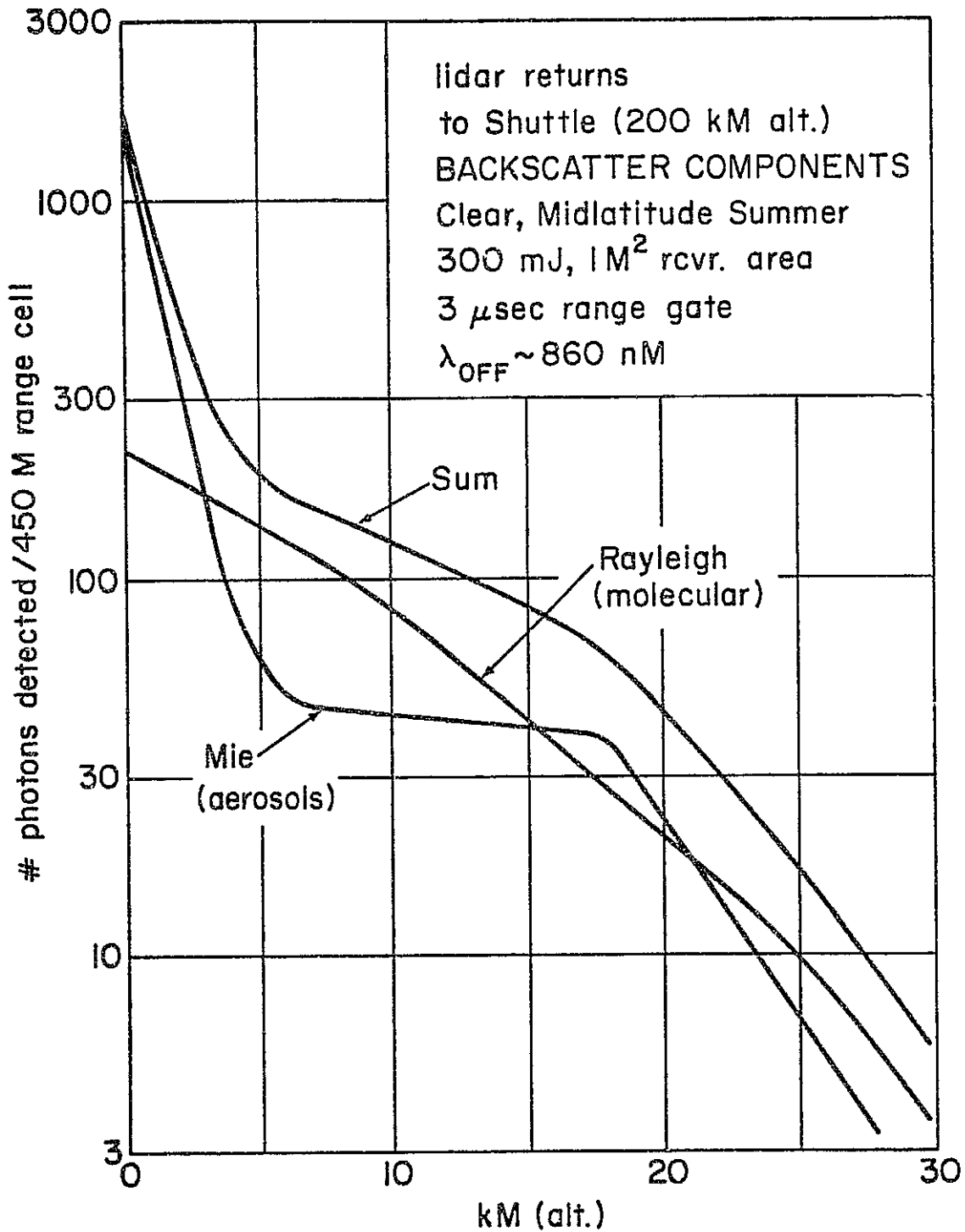


Figure 27

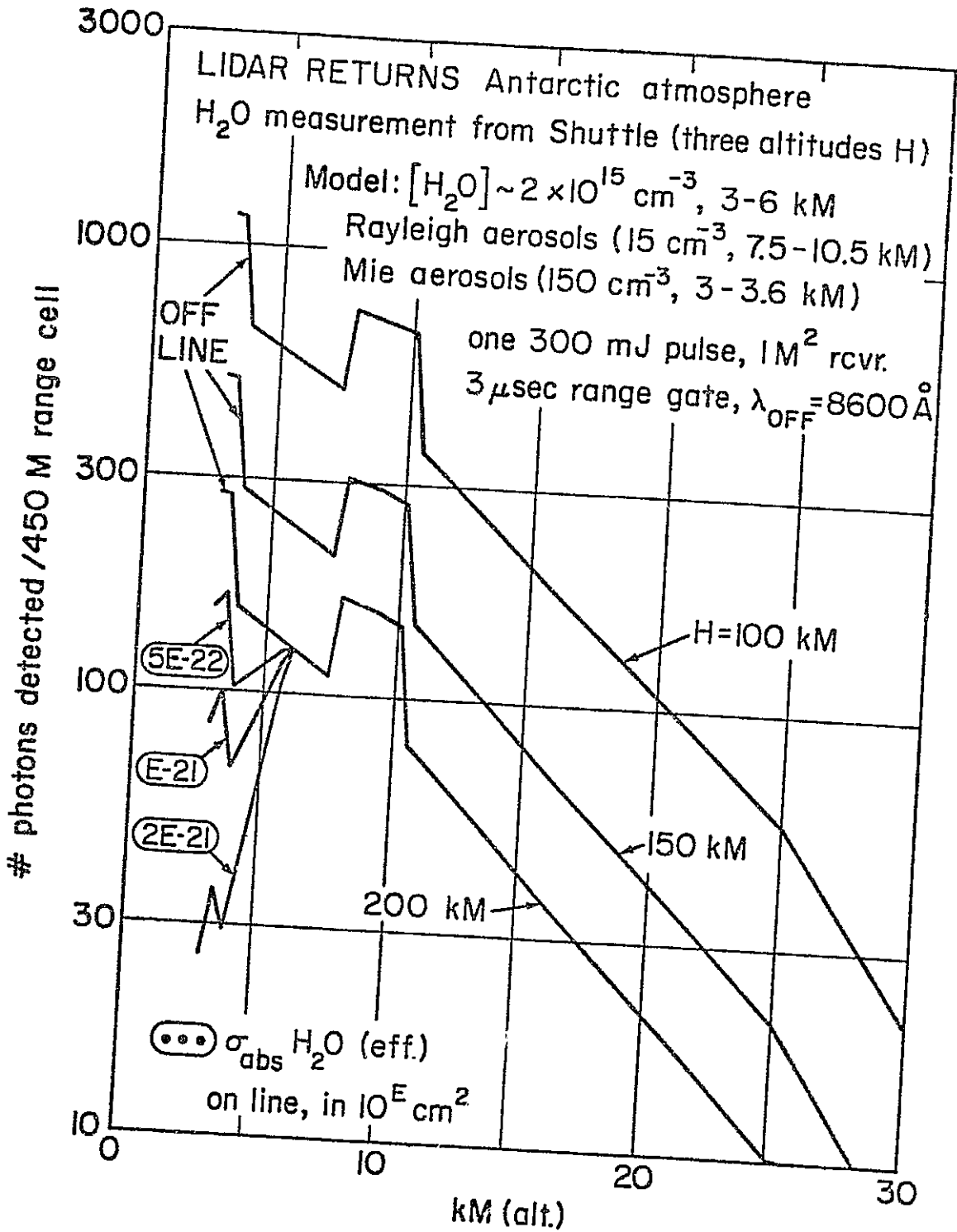


Figure 28

are needed. Since the ground return will be a large signal, total column content of H_2O constitutes an attractive measurement under these conditions.

The importance of knowing $[H_2O]$ in the polar atmosphere is due in part to the scavenging of airborne, condensible pollutants which probably takes place there. The precipitation of water vapor as high altitude ice crystals must play a role in any such process. The capability of a Shuttle-based lidar to see both the vapor and condensed phases of H_2O will be important in understanding polar precipitation. There may be no other method for wide area studies of this problem in remote regions of the earth.

3.4 Accuracy and Practicality of Orbital Lidar for $[H_2O]$

This section summarizes the available information on the accuracy with which the concentration of tropospheric water vapor may be measured via orbital lidar. Since our simulations do not contain an explicit error analysis, we rely on related calculations which are known to yield lidar returns comparable in magnitude to those presented here. The main source of error is signal shot noise, due to the number of detectable photons lying within a given range gate, combined with the logarithmic derivative operation (Equation 6) which is required for obtaining material concentration from the lidar returns. For a finite range resolution Δr , this is equivalent to a double ratio of four signals: the on line and off line returns from both the top and bottom of the range cell of interest.

Remsberg et al (1975) have studied the general performance of differential absorption lidars, particularly in the favorable wavelength range $3000 \overset{\circ}{\text{A}} - 1$ micron which includes all the water line groups discussed in this report. They conclude:

"Better than 10% measurements of material concentrations are possible below about 15 km for 10J/pulse laser energies. In the wavelength region $0.3 < \lambda < 1.0 \mu\text{M}$, oxygen, water vapor and possibly NO_2 can thus be measured in the troposphere."

This conclusion assumes: Shuttle altitude = 200 km, telescope area = 1 M^2 , overall detection efficiency = 10% (as in the present report), and a height resolution of 2 km.

We can compare this estimate with one scaled from the SRI report by Wright et al (1975) on lidar measurements of atmospheric pollutants such as NO_2 , using as a scaling factor the available spectral contrast $[\sigma(\lambda_0) - \sigma(\lambda)]$ (Equation 6). This is approximately $3 \times 10^{-19} \text{ cm}^2$ for NO_2 around 4500 A according to Wilkerson et al (1974), whereas we may take it as roughly 10^{-23} cm^2 for H_2O lines discussed in the present report which yield distinct on line returns (e.g., see Figure 22). Since the SRI estimate of minimum detectable $[\text{NO}_2]$ is equivalent to 0.01 ppm for a single 10J lidar pulse pair, the related quantity for H_2O is $10^{-2} \text{ ppm} \times 3 \times 10^{-19} / 10^{-23} = 300 \text{ ppm}$. Moreover, since the typical H_2O abundance is of order 10^4 ppm , the minimum detectable variation in $[\text{H}_2\text{O}]$ is therefore approximately $300 / 10^4 = 3\%$ under the given lidar assumptions.

Further, Remsberg et al continue:

"... more detailed simulations were conducted for water vapor in the $0.72 \mu\text{M}$ region using a 0.1J/pulse laser operating at 1 pps. Relative humidity data accurate to 4% can be obtained from a Shuttle platform for a 0.5 km range cell near the surface and for horizontal grids of 250 km."

These lidar conditions are equivalent to about 4J total energy output during

the Shuttle transit over the horizontal grid spacing, or about 1 Joule for a 4 x larger vertical range cell of 2 km. That this laser energy estimate for 4% relative humidity accuracy is about 1/10 of that extrapolated from the SRI results on [NO₂] is encouraging, and may reflect the noticeably greater off line scattering extinction at 4500 Å as opposed to 7200 Å.

It is clear that integrated laser pulse energies of order 3J will be needed for tropospheric water vapor observations with a 1 M² telescope in the Shuttle, in order to obtain ~1 km vertical resolutions and relative humidity accuracy better than 5%. Since 300 mJ pulses can be expected with a 3J pump laser and 10% conversion efficiency, this would require 10 pulses - or a 10 M² receiver in the case of one 300 mJ tunable, near IR pulse. Very large receiving telescopes have indeed been considered for the Shuttle, and we would conclude that they should be made available for lidar measurements in order that the maximum useful information on the atmosphere be obtained.

In conclusion, one can write a criterion for useful near IR lidar measurements (Shuttle altitude = 200 km) giving relative humidities accurate to roughly 3% at low altitudes in the atmosphere, namely:

$$N \cdot E \cdot A \cdot K \cdot \Delta R \geq 3 \times 10^2 \text{ J} \cdot \text{M}^3, \quad (15)$$

(near IR, N pulses, 3% humidity accuracy)

where ΔR is the height resolution (lidar range cell), A is the receiving telescope area, K is the overall detection efficiency, E is transmitted laser energy per pulse, and N is the number of lidar pulses accumulated for a given observation.

Another criterion may be written for the average electrical power \bar{P} (watts) required by the lidar apparatus during a time interval of observation which covers a horizontal distance D (meters) at ground level:

$$\eta \bar{P} \cdot D \cdot A \cdot K \cdot \Delta R \geq 2 \times 10^6 \text{ W} \cdot \text{M}^4, \quad (16)$$

where η is the conversion efficiency from electrical power into average lidar output power. This relationship roughly accounts for the ground speed of the Shuttle (~ 7 km/sec) and the estimate (above) that the product $\eta \bar{P}$ must be of order 3J.

An example of the consequences of these criteria is important to cite in closing this section. For mesoscale observations (Section 2) it is preferable to have a horizontal resolution capability of order 1/10 the size of 100 km spatial variations; i.e., set $D = 10$ km. Given a detection efficiency $K = 10\%$ and a height resolution $\Delta R = 1$ km, this requires $\eta \bar{P} \cdot A = 2 \text{ WM}^2$. For an average electrical power of 1 kW dedicated to the Shuttle Lidar Facility, and $\eta = 10^{-3*}$, the required receiver area is 2 M^2 ; this is considered to be a reasonable value by most lidar design groups.

Thus a Shuttle-based water vapor lidar instrument appears to be practical. The magnitude of the atmospheric returns and the absorption strengths of resolvable H_2O lines are large enough for useful meteorological studies of the altitude distribution of water vapor. Moreover, an orbital lidar probably is the only means for worldwide surveys of tropospheric H_2O , including many remote regions of the earth.

* This figure mediates between the value of 5×10^{-4} we estimate as reasonable for proven laser systems and 3×10^{-3} which may soon be possible with excimer-laser-pumped tunable lasers.

4. Exploratory Laser Experiments

This section describes experiments undertaken at the University of Maryland to explore the application of various dye laser methods for generating laser pulses which could be tuned over H₂O absorption lines in the visible and near infrared. The work reported here is the basis for subsequent laser developments under NASA grant NSG - 1156, which have been summarized by McIlrath et al (1975) and Wilkerson et al (1975) and will be described in greater detail in the near future. Here we report on the following:

- (4.1) Operation of a long pulse dye laser (10^{-6} sec full width at base) with a tunable, narrow band output at high energies near the 5915 Å water vapor absorption bands.
- (4.2) Assembly and operation of a short duration dye laser (2×10^{-7} sec full width at base) near the 5915 Å water vapor absorption bands.
- (4.3) Construction of a dye laser to be pumped by the lasers in (1) and (2) above to operate in the red and near infrared. This laser has operated in the region of the 6513 Å and the 6981 Å absorption bands.
- (4.4) Preliminary studies of the beam divergence of the output of the laser-pumped system.

In the rest of this section we discuss these results in more detail. They are summarized in Section 4.5.

4.1 Operation of Long Pulse Dye Laser

The long pulse dye laser is a high energy system capable of 1.25 Joules output in a 10^{-6} second pulse. We have used it in a cavity with a diffraction

grating as the tuning element and have kept the output energies below 0.4 Joules. No grating damage was observed. Using Rhodamine 6G dissolved in methanol we tuned to 5900 \AA with a line width of $< 1 \text{ \AA}$. The beam divergence was studied by photographing the beam with a four lense camera to get the intensity distribution at various distances from the output. Preliminary measurements indicate that the central core of the beam had a divergence of less than 6×10^{-3} rad. This system is now being used in conjunction with a sodium vapor heat pipe oven to tune onto the narrow sodium resonance lines at 5890 \AA . Observations of resonance scattering for many shots should give a good indication of shot-to-shot spectral stability in this configuration. Tuning through the resonance lines will also give a measure of the spectral width.

4.2 Short Pulse Flashlamp-Pumped Laser

A flashlamp-pumped dye laser using a Marx Bank capacitor storage was put into operation. Outputs of 184 mj were obtained in the 5800 \AA region using Rhodamine 6G in methanol. It would be possible to obtain 250 mj of energy by optimizing the dye concentration. The pulse width is less than 250×10^{-9} seconds at the base and 10^{-7} seconds at half maximum giving an output power of 2×10^6 watts. This system was also operated with cresyl violet to obtain output at longer wavelengths. The output mode structure was complicated, as expected, and the flashlamp-pumped dye laser is used mainly as a pump for the laser-pumped dye laser. Direct output of the cresyl violet dye laser was 45 mj with no effort made to optimize the output.

4.3 Laser-Pumped Dye Laser with Cresyl Violet

A dye laser was constructed consisting of a stainless steel dye cell, a total reflector, and an output coupling reflector. The cell is designed to be driven by the output of a flashlamp-pumped laser, either dye or ruby. The laser was operated with cresyl violet in methanol and pumped by the output of the fast pulsed laser operating with Rhodamine 6G. Conversion efficiencies of 4% were achieved without efforts at optimizing. The output of cresyl violet is near 6500 Å. Photographs of the output beam show a beam divergence of less than 2×10^{-3} rad.

4.4 Laser-Pumped Dye Laser with Nile Blue Perchlorate

The laser-pumped dye laser was operated with a solution of Nile Blue Perchlorate in Methanol. This system lased well with an output of 1.2 mj centered on 6932 Å. The output should be increased by changing the pump wavelength and dye solvent and by optimizing the dye concentration. The mode pattern is similar to the cresyl violet case.

4.5 Summary

Enough information has been gathered to allow construction of a tunable dye laser operating in the near infrared region which is suitable for differential absorption Lidar experiments. Water vapor absorption lines in the 7150 - 7400 Å region and the 8100 - 8400 Å region offer a wide variety of line strengths and can easily be reached with tunable dye lasers (see Section 3.2). The H₂O absorption lines are approximately .07 Å in width, a width which again is easily matched by dye lasers. The next step in this work has been the construction of such a tunable dye laser that is adequate for prototype experiments.

For ease of construction, a dye laser pumped by a giant pulsed ruby laser is most attractive. Experiments on such a laser are currently underway under NSG-1156. Sufficiently energetic and spectrally pure pulses are now available for "ground truth" measurements of atmospheric water vapor, according to simulations of the kind represented by Figure 19. The ease of reaching this experimental configuration assures us that the laser parameters needed for Shuttle observations of H_2O can readily be obtained with space-qualified instruments during the late 1970's. This further buttresses the case for the practicality of orbital H_2O lidar from the Space Shuttle platform.

Appendix 1

The relationship between different meteorological
parameters used to specify the water
vapor content of air

It is useful to briefly discuss the parameters used by meteorologists to denote the water vapor content of air. The most commonly used parameters are:

1. Mixing ratio $\omega \equiv \rho_v / \rho_d$
 ρ_v - water vapor density
 ρ_d - Density of dry air containing the water vapor
2. Specific humidity $q \equiv \rho_v / \rho_a$
 ρ_a - density of moist air containing the water vapor
 $q = \omega / (1 + \omega)$
3. Percent Relative humidity $r = 100 e / e_s(T)$
 e - water vapor partial pressure
 e_s - saturation vapor pressure with respect to a plane liquid water surface at the temperature, T , of the vapor.
4. Absolute humidity ρ_v

It should be noted that ω and q are conservative properties of air undergoing dry adiabatic processes. Thus, these parameters serve as convenient tracers of air for many atmospheric problems.

The absolute humidity or water vapor density is used less than ω , q or r . However, ρ_v or the number density N_v is the variable obtained from the lidar retrieval technique. The water vapor data requirements

discussed refer to relative humidity. The material below relates relative humidity to water vapor density.

Assuming water vapor obeys the ideal gas law, one may relate r to ρ_v by the following equation.

$$r = 100 \rho_v \frac{R_w T}{e_s(T)}$$

where R_w is the gas constant for water vapor.

Let r_0 , ρ_{v0} and T_0 be the correct values of r , ρ_v and T , respectively, and let δr , $\delta \rho_v$ and δT be the uncertainty of r , ρ_v and T , respectively. Assuming the Clausius-Clapeyron equation is approximately correct for finite temperature differences, then the fractional error of relative humidity can be related to the fractional error in density and temperature by the equation

$$\frac{\delta r}{r_0} = \frac{\delta \rho_v}{\rho_{v0}} + \left(1 - \frac{L_v}{R_w T_0}\right) \frac{\delta T}{T_0}$$

where L_v is the latent heat of vaporization.

It is easily seen that the relative error in r equals the relative error in ρ_v when the temperature is known precisely. However, if the temperature uncertainty gets large, it will mask the effects of the water vapor uncertainty.

At $T = 0^\circ\text{C}$, the term $\left(1 - \frac{L_v}{R_w T_0}\right) \frac{\delta T}{T_0}$ amounts to -0.068 , -0.344 , -0.688 , for $\delta T = 1.0$, 5.0 and 10.0°C , respectively. This effect of the temperature uncertainty should not be overlooked when estimating the uncertainty in relative humidities obtained from water vapor density estimates.

References

- Ahmed, S. A., 1973: Applied Optics, 12, 901.
- Bengtsson, L. and N. Gustavsson, 1972: Assimilation of non-synoptic observations. Tellus, 24, 383-399.
- Belts, A. K., F. J. Dugan, and R. W. Grover, 1974: Residual errors of the VIZ radiosonde hygistor as deduced from observations of sub-cloud layer structure. Bull. Amer. Meteor. Soc., 55, 1123-1125.
- Betts, A. and D. Rodenhuis, 1974: The Convection Sub-programme for the GARP Atlantic Tropical Experiment. GATE Rept. No. 7, World Meteorological Organization, Geneva, 83pp.
- Bourke, P. M. A., 1955: The forecasting from weather data of potato blight and other plant disease pests. WMO Technical Note No. 10, 49pp.
- Brousaides, F. J., 1975: The radiosonde hygistor and low relative humidity measurements. Bull. Amer. Meteor. Soc., 56, 229-233.
- Byer, R. L., and M. Garbuny, 1973: Applied Optics, 12, 1496.
- Compendium of Meteorological Satellites and Instrumentation, 1973: National Space Science Data Center Report NSSDC 73-02, 455pp.
- Doös, B. R., 1970: Numerical Experimentation related to GARP. GARP Publication Series, No. 6, World Meteorological Organization, Geneva, 68pp.
- Farmer, C. B., 1970: The strengths of H₂O lines in the 8200 Å region and their application to high dispersion spectra of Mars, Icarus, 15, 190-196.
- Foote, G. B., and J. C. Fankhauser, 1973: Air flow and moisture budget beneath a northeast Colorado hailstorm. J. Appl. Meteor., 12, 1330-1353.

- Friedman, M., 1972: A new radiosonde case: The problem and the solution. Bull. Amer. Meteor. Soc., 53, 884-887.
- GARP Joint Organizing Committee, 1974: Modeling for the first GARP Global Experiment. GARP Publication Series, No. 14, World Meteorological Organization, Geneva, 261pp.
- Kuettner, J. P., D. E. Parker, D. R. Rodenhuis, H. Holber, H. Kraus, and G. Philander; 1974: GATE final international scientific plans. Bull. Amer. Meteor. Soc., 55, 711-744.
- Lenhard, R. W., 1970: Accuracy of radiosonde temperature and pressure-height determination. Bull. Amer. Meteor. Soc., 51 842-846.
- Lenschow, D. H., and E. M. Agee, 1974: The Air Mass Transformation Experiment (AMTEX): Preliminary results from 1974 and plans for 1975. Bull. Amer. Meteor. Soc., 55, 1228-1235.
- Lilly, D., 1975: Project SESAME planned. Bull. Amer. Meteor. Soc., 56, 16.
- Manual for the Radiosonde Code, 1963: U. S. Dept. of Commerce, 58pp.
- Mastenbrook, H. J., 1966: Water vapor measurements at low, middle and high latitudes during 1964 and 1965. U. S. Naval Research Laboratory, NRL Rept. 6447, 199pp.
- Mastenbrook, H. J., 1971: Variability of water vapor in the stratosphere. J. Atmo. Sci., 28, 1495-1501.
- McClatchey, R. A., R. W. Fenn, J. E. A. Selby, F. E. Volz and J. S. Garing, 1970: Optical Properties of the Atmosphere, AFCRL Environmental Research Paper, No. 331, 85pp.

- McClatchey, R. W., R. W. Fenn, J. E. A. Selby, F. E. Volz and J. S. Garing, 1972: Optical Properties of the Atmosphere (Third Edition), Air Force Cambridge Research Laboratory Report No. 72-0497, 108pp.
- McIlrath, T. J., M. B. Morris and R. W. Gammon, 1975: Tunable laser for water vapor lidar, Proceedings, 7th International Laser Radar Conference, (SRI, Menlo Park, Ca.), 29-30.
- Measures, R. M., and Gilles Pilon, 1972: Opto-electronics 4, 141.
- Meredith, R. E., T. S. Chang, F. G. Smith and D. R. Woods, 1973: Investigations of Molecular Absorption Line Parameters for Constituents, Science Applications Inc. Report No. SAI-73-004-AA(II) on ARPS/STO Contract No. DAAH-01-73-C-0786.
- Morrissey, J. F., and F. J. Broussides, 1970: Temperature induced errors in the ML-476 humidity data. J. Appl. Meteor., 9, 805-808.
- Ostapoff, F., W. Skinners, and E. Augstein, 1970: Some tests on the radiosonde humidity error. NOAA Technical Report ERL 195-AOML 4.
- Ostapoff, F., W. Skinners, and E. Augstein, 1973: A revised assessment of radiosonde accuracy. Bull. Amer. Meteor. Soc., 54, 691-693.
- Quiring, R. F., 1973: Low humidity still a problem with the modified NWS radiosonde? Bull. Amer. Meteor. Soc., 54, 551-552.
- Remsberg, E. E., L. Gordley, S. K. Poultney and R. T. Thompson, 1975: Analysis of differential absorption lidar measurements from space shuttle, Proceedings, 7th International Conference on Laser Radar (SRI, Menlo Park, Ca.), 20-21.

- Rhea, J. O., 1966: A study of thunderstorm formation along dry lines. *J. Appl. Meteor.*, 50, 58-63.
- Rutherford, I. D., 1972: Data assimilation by statistical interpolation of forecast error fields. *J. Atmos. Sci.*, 29, 809-815.
- Schaefer, J. T., 1974a: A simulative model of dryline motion. *J. Atmos. Sci.*, 31, 956-964.
- Schaefer, J. T., 1974b: The life cycle of the dryline. *J. Appl. Meteor.*, 13, 444-449.
- Schaefer, J. T., 1974c: News and Notes. *Bull. Amer. Meteor. Soc.*, 55, 1379.
- Selected Climatic Maps of the United States, 1965: U. S. Dept. of Commerce, Environmental Data Service, 32pp.
- Swensson, J. W., W. S. Benedict, L. Delbouille and G. Roland, 1970: The Solar Spectrum from λ 7498 to λ 12016, Institut d'Astrophysique de l'Universite de Liege.
- Teweles, S., 1970: A spurious diurnal variation in radiosonde humidity records. *Bull. Amer. Meteor. Soc.*, 51, 836-840.
- U. S. Standard Atmosphere Supplements, 1966: 289pp.
- Wallin, J. R. 1967: Ground level climate in relation to forecasting plant diseases. *Ground level climatology*, Washington, D. C. AAAS, 149-163.
- Weather Station Index, 1965: U. S. Naval Oceanographic Office, H. O. Pub. No. 119.
- Weller, G., and E. W. Bierly, 1973; The Polar Experiment (POLEX). *Bull. Amer. Meteor. Soc.*, 54, 212-218.

- Wilkerson, T. D., B. Ercoli and F. S. Tomkins, 1974: Absorption Spectra of Atmospheric Gases, Univ. of Maryland and Argonne National Laboratory Report No. BN-784 to Stanford Research Institute on Project 935536-13GZ, 93pp.
- Wilkerson, T. D., L. Cotnoir and G. Schwemmer, 1975: Water vapor lidar: calibration and simulation, Proceedings, 7th International Conference on Laser Radar (SRI, Menlo Park, Ca.), 31-32.
- Wolfe, W. L., (Ed.), 1965: Handbook of Military Infrared Technology, publ. at USGPO for Office of Naval Research.
- Wright, M. L., E. K. Proctor, L. S. Gasiorok, and E. M. Liston, 1975: A Preliminary Study of Air Pollution Measurement by Active Remote Sensing Techniques, Stanford Research Institute Report on Contract NAS 1-11657, NASA CR-132724.
- Yates, H. W., and J. H. Taylor, 1960: Infrared Transmission of the Atmosphere, USNRL Report No. 54, ASTIA Document No. AD 240188.
-
- Schotland, Richard M., 1966: Some observations of the vertical profile of water vapor by a laser optical radar, Proceedings of the 4th Symposium on Remote Sensing of the Environment (April, 1966) University of Michigan, 273-283.
- Schotland, Richard M., 1974: Errors in the lidar measurement of atmospheric gases by differential absorption, J. Appl. Meteorology 13, 71-77.